Precision thrust cumulant moments at N[superscript 3]LL

Precision thrust cumulant moments at N^{3}LL

Riccardo Abbate,[1] Michael Fickinger,[2] André H. Hoang,[3] Vicent Mateu,[1,4] and Iain W. Stewart[1]

[1]*Center for Theoretical Physics, Massachusetts Institute of Technology, Cambridge, Massachusetts 02139, USA*
[2]*Department of Physics, University of Arizona, Tucson, Arizona 85721, USA*
[3]*Faculty of Physics, University of Vienna, Boltzmanngasse 5, 1090 Vienna, Austria*
[4]*IFIC, UVEG-CSIC, Apartado de Correos 22085, E-46071, Valencia, Spain*
(Received 28 May 2012; published 1 November 2012)

We consider cumulant moments (cumulants) of the thrust distribution using predictions of the full spectrum for thrust including $\mathcal{O}(\alpha_s^3)$ fixed order results, resummation of singular N^{3}LL logarithmic contributions, and a class of leading power corrections in a renormalon-free scheme. From a global fit to the first thrust moment we extract the strong coupling and the leading power correction matrix element Ω_1. We obtain $\alpha_s(m_Z) = 0.1140 \pm (0.0004)_{\rm exp} \pm (0.0013)_{\rm hadr} \pm (0.0007)_{\rm pert}$, where the 1-$\sigma$ uncertainties are experimental, from hadronization (related to Ω_1) and perturbative, respectively, and $\Omega_1 = 0.377 \pm (0.044)_{\rm exp} \pm (0.039)_{\rm pert}$ GeV. The nth thrust cumulants for $n \geq 2$ are completely insensitive to Ω_1, and therefore a good instrument for extracting information on higher order power corrections, Ω_n'/Q^n, from moment data. We find $(\tilde{\Omega}_2')^{1/2} = 0.74 \pm (0.11)_{\rm exp} \pm (0.09)_{\rm pert}$ GeV.

DOI: 10.1103/PhysRevD.86.094002 PACS numbers: 12.38.−t, 12.38.Cy, 13.66.Jn

I. INTRODUCTION

The process $e^+e^- \to$ jets plays an important role in precise determinations of $\alpha_s(m_Z)$, as well as for probing the nonperturbative dynamics of hadronization in jet production. A wealth of high precision data with percent level uncertainties is available for jet production in e^+e^- collisions at the Z pole, $Q = m_Z$, and with somewhat larger uncertainties at both lower and higher energies Q. For a review of classic work on $\alpha_s(m_Z)$ determinations using event shapes and other jet observables, the reader is referred to Ref. [1]. Accurate predictions for event shapes are now available which include $\mathcal{O}(\alpha_s^3)$ corrections [2–5], a next-to-next-to-next-to-leading-log (N^{3}LL) resummation of large logarithms [6,7], and a high precision method developed for simultaneously incorporating field theory matrix elements for the power corrections [8].

The majority of fits for $\alpha_s(m_Z)$ from event shapes e make use of cross section distributions $\mathrm{d}\sigma/\mathrm{d}e$, in a region where nonperturbative effects enter as power corrections in $1/Q$ and the theoretical description is the most accurate. In our recent analysis [8] for the event-shape variable thrust $\tau = 1 - T$ [9],

$$T = \max_{\hat{\mathbf{t}}} \frac{\sum_i |\hat{\mathbf{t}} \cdot \vec{p}_i|}{\sum_i |\vec{p}_i|}, \qquad (1)$$

we obtained a precise determination of $\alpha_s(m_Z)$. Our theoretical description is based on soft-collinear effective theory [10–14], and has several advanced features, such as

(1) Matrix elements and nonsingular terms at order α_s^3 using results from Ref. [2]. Nonlogarithmic terms in the hard function are included at order α_s^3 as well.
(2) Resummation of the singular logarithmic terms to all orders in α_s up to N^{3}LL order.
(3) Profile functions (τ-dependent scales μ_J, μ_S, R, $\mu_{\rm ns}$) that correctly treat the peak region and account for the multijet boundary condition to ensure that predictions converge properly into the known fixed order result in the multijet endpoint region. They allow an accurate theoretical description over the entire range $\tau \in [0, 0.5]$.
(4) Description of nonperturbative effects with field theory and a fit to a single nonperturbative matrix element of Wilson lines Ω_1 in the tail region [where power corrections are described by an operator product expansion (OPE)].
(5) Definition of Ω_1 in a more stable Rgap scheme [15,16] rather than in $\overline{\rm MS}$. This ensures Ω_1 and the perturbative cross section are free of $\mathcal{O}(\Lambda_{\rm QCD})$ renormalon ambiguities. An renormalization group equation (RGE) is used to sum large logarithms in the perturbative renormalon subtractions [17,18]. The fit gives Ω_1 with an accuracy of 16%.
(6) QED final state corrections at $\mathcal{O}(\alpha)$ and next-to-next-to-leading logarithm (NNLL) (counting $\alpha \sim \alpha_s^2$); bottom mass corrections are included using a factorization theorem with log resummation; $\mathcal{O}(\alpha_s^2)$ axial-singlet terms arising from the large top-bottom mass splitting are included as well.

A two-parameter global fit in the tail of the thrust distribution gives [8] $\alpha_s(m_Z) = 0.1135 \pm (0.0002)_{\rm exp} \pm (0.0005)_{\rm hadr} \pm (0.0009)_{\rm pert}$ as well as $\Omega_1 = 0.323 \pm (0.009)_{\rm exp} \pm (0.013)_{\Omega_2} \pm (0.020)_{\alpha_s(m_Z)} \pm (0.045)_{\rm pert}$ GeV where $\Omega_1 \equiv \Omega_1(R_\Delta, \mu_\Delta)$ is defined in the Rgap scheme at the scales $R_\Delta = \mu_\Delta = 2$ GeV. For α_s the three uncertainties are the experimental uncertainty, hadronization uncertainty coming mainly from the determination of Ω_1, and the perturbative theoretical uncertainty. This result for α_s is one of the most precise in the literature. It is also one of the lowest, being 3.9σ away from the 2009 world average [19] and 4.0σ from the 2011 world average [20]. For a detailed discussion of $\alpha_s(m_Z)$ determinations, see Ref. [21]. The small value of $\alpha_s(m_Z)$ is directly connected to the nonnegligible correction from Ω_1 [8], whose fit value is of natural size $\Omega_1 \sim \Lambda_{\rm QCD}$. Given the discrepancy, further tests of the theoretical predictions for event shapes are warranted. In this paper, we will do so using experimental moments involving the thrust variable.

The property of the $\mathrm{N^3LL} + \mathcal{O}(\alpha_s^3)$ predictions for $\mathrm{d}\sigma/\mathrm{d}\tau$ in Ref. [8] that we will exploit is that they are valid in both the dijet and tail regions, where singular and large logarithmic terms in need of resummation arise, and in the multijet region, where fixed order results without log resummation should be used. That is, they are valid for all values of τ (an improvement over earlier results at this order). Important ingredients are: the inclusion of the nonsingular terms, important away from the peak region; the use of profile functions that turn off resummation in the far-tail region; and the inclusion of a soft function, which is necessary to describe the peak in the dijet region, where nonperturbative effects are $\mathcal{O}(1)$.

We will use the full τ range results to analyze moments M_n of the thrust distribution in $e^+e^- \to$ jets,

$$M_n = \frac{1}{\sigma}\int_0^{\tau_{\rm max}=1/2} \mathrm{d}\tau\,\tau^n \frac{\mathrm{d}\sigma}{\mathrm{d}\tau}. \tag{2}$$

Unlike for tail fits, the entire physical τ range contributes, providing sensitivity to a different region of the spectrum. Experimental results are available for many values of Q, and the analysis of systematic uncertainties is to a large extent independent from that for the binned distributions. Thus the outcome for a fit of data for the first moment M_1 to $\alpha_s(m_Z)$ and Ω_1 serves as an important cross check of the results obtained in Ref. [8]. The M_n moments are also not sensitive to large logarithms, and hence provide a nontrivial check on whether the $\mathrm{N^3LL} + \mathcal{O}(\alpha_s^3)$ full spectrum results, which contain a summation of logarithms of τ with a substantial numerical effect for small τ values, can reproduce this property. We explore this issue both for central values and for theory uncertainty estimates.

The second purpose of this work is to discuss the structure of higher order power corrections in thrust moments. We find that cumulant moments M_n' (cumulants) are very useful, since they allow for a cleaner separation of the subleading nonperturbative matrix elements compared to the M_n moments of Eq. (2). Cumulants include the variance M_2' and skewness M_3', and we will consider the first five:

$$\begin{aligned}
M_1' &= M_1,\\
M_2' &= M_2 - M_1^2,\\
M_3' &= M_3 - 3M_2M_1 + 2M_1^3,\\
M_4' &= M_4 - 4M_3M_1 - 3M_2^2 + 12M_2M_1^2 - 6M_1^4,\\
M_5' &= M_5 - 5M_4M_1 - 10M_3M_2 + 20M_3M_1^2\\
&\quad + 30M_2^2M_1 - 60M_1^3M_2 + 24M_1^5.
\end{aligned} \tag{3}$$

In the leading order thrust factorization theorem the power correction matrix elements for the moments M_n are called Ω_m while for the cumulants M_n' they are called Ω_m'. [The Ω_m' are also related to the Ω_m by Eq. (3) with $M_n \to \Omega_n$]. In particular, the invariance of the cumulants to shifts in τ implies that the $M_{n\ge2}'$ moments are completely insensitive to the leading thrust power correction parameter Ω_1, and hence can provide nontrivial information on the higher order power corrections which enter as Ω_n'/Q^n and as $1/Q^2$ power corrections from terms beyond the leading factorization theorem. In contrast, for each $M_{n\ge2}$ there is a term $\sim\alpha_s\Omega_1/Q$ that for larger Qs dominates over the Ω_m/Q^m terms.[1]

A. Review of experiments and earlier literature

Dedicated experimental analyses of thrust moments have been reported by various experiments: JADE [22] measured the first moment at $Q = 35$, 44 GeV, and in Ref. [23] reported measurements of the first five moments at $Q = 14$, 22, 34.6, 35, 38.3, 43.8 GeV; OPAL [24] measured the first five moments at $Q = 91$, 133, 177, 197 GeV, and there is an additional measurement of the first moment at $Q = 161$ GeV [25]; ALEPH [26] measured the first moment at $Q = 91.2$, 133, 161, 172, 183, 189, 196, 200, 206 GeV; DELPHI [27] has measurements of the first moment at $Q = 45.2$, 66, 76.3 GeV, measurements of the first three moments at $Q = 183$, 189, 192, 196, 200, 202,205, 207 GeV [28], and at $Q = 91.2$, 133, 161, 172, 183 GeV [29]; L3 [30] measured the first two moments at $Q = 91.2$ GeV and other center of mass energies which are superseded by the ones in Ref. [31] at $Q = 41.4$, 55.3, 65.4, 75.7, 82.3, 85.1, 130.1, 136.1, 161.3, 172.3, 182.8, 188.6, 194.4, 200.2, 206.2 GeV; TASSO measured the first moment at $Q = 14$, 22, 35, 44 GeV [32]; and AMY measured the first moment at $Q = 55.2$ GeV [33]. Finally, the variance and skewness have been explicitly measured by DELPHI [29] at $Q = 133$, 161, 172, 183 GeV; and OPAL [25] at $Q = 161$ GeV. All of the experimental moments will be used in our fits, with the exception of the results in Ref. [23] and data

[1]The cumulants begin to differ for $n \ge 4$ from the so-called central moments, $\langle(\tau - M_1)^n\rangle$. Both cumulants and central moments are shift independent, but the cumulants are slightly preferred because they are only sensitive to a single moment of the leading order soft function in the thrust factorization theorem.

with $Q \leq 22$ GeV where our treatment of b-quark mass effects may not suffice.

In principle the JADE results in Ref. [23] supersede the earlier analysis of this data reported in Ref. [22]. In the more recent analysis the contribution of primary $b\bar{b}$ events has been subtracted using Monte Carlo generators.[2] Since the theoretical precision of these generators is significantly worse than our N^{3}LL + $\mathcal{O}(\alpha_s^3)$ treatment of massless quark effects and our NNLL + $\mathcal{O}(\alpha_s)$ treatment of m_b-dependent corrections, it is not clear how our code should be modified consistently to account for these subtractions. Comparing the old versus new JADE data at $Q = 44$ GeV one finds $M_1 = 0.0860 \pm 0.0014$ versus $M_1 = 0.0807 \pm 0.0016$. This corresponds to a 3.4σ change assuming 100% correlated uncertainties (or a 2.6σ change with uncorrelated uncertainties). In our analysis we find that the older JADE data provides more consistent results when employed in a combined fit with data from the other experiments (related to smaller χ^2 values). For this reason our default data set incorporates only the older JADE moment data. We will report on the change that would be induced by using the new JADE data if we simply ignore the fact that the $b\bar{b}$ events were removed.

Event-shape moments have also been extensively studied in the theoretical literature. The $\mathcal{O}(\alpha_s^3)$ QCD corrections for event-shape moments have been calculated in Refs. [34,35]. The leading Λ/Q power correction to the first moment of event-shape distributions were first studied in Refs. [36–39] often with the study of renormalons (see Ref. [40], and Ref. [41] for a review). Reference [42] made a renormalon analysis of the second moment of the thrust distribution, finding that the leading renormalon contribution is not $1/Q^2$ but rather $1/Q^3$. Hadronization effects have also been frequently considered in the framework of the dispersive model for the strong coupling [36,43,44].[3] In this approach, an IR cutoff μ_I is introduced and the strong coupling constant below the scale μ_I is replaced by an effective coupling $\alpha_{\rm eff}$ such that perturbative infrared effects coming from scales below μ_I are subtracted. In the dispersive model the term $\mu_I \alpha_0$ is the analog of the QCD matrix element Ω_1 that is derived from the OPE. Since in the dispersive model there is only one nonperturbative parameter, it does not contain analogs of the independent nonperturbative QCD matrix elements $\Omega_{n\geq 2}$ of the operator product expansion. Thus measurements of $\Omega'_{n\geq 2}$ can be used as a test for additional nonperturbative physics that go beyond this framework.

The dispersive model has been used in Refs. [24,46,47] together with $\mathcal{O}(\alpha_s^2)$ fixed order results to analyze event-shape moments, fitting simultaneously to $\alpha_s(m_Z)$ and α_0. Recently these analyses have been extended to $\mathcal{O}(\alpha_s^3)$ in Ref. [48], based on code for $n_f = 5$ massless quark flavors, using data from Refs. [23,24] and fitting to the first five moments for several event-shape variables. Our numerical analysis only considers thrust moments, but with a global data set from all available experiments. A detailed comparison with Ref. [48] will be made at appropriate points in the paper. Theoretically our analysis goes beyond their work by using a formalism that has no large logarithms in the renormalon subtraction, includes the analog of the "Milan factor" [44,49] in our framework at $\mathcal{O}(\alpha_s^3)$ (one higher order than Ref. [48]), and incorporates higher order power corrections beyond the leading shift from Ω_1. We also test the effect of including resummation.

B. Outline

This article is organized as follows: We start out by defining moments and cumulants of distributions, and their respective generating functions in Sec. II, where we also discuss the leading and subleading power corrections of thrust moments in an OPE framework. In Sec. III, we present and discuss our main results for $\alpha_s(m_Z)$ from fits to the first thrust moment M_1. In Sec. VI, we analyze higher moments $M_{n\geq 2}$. Section VII contains an analysis of subleading power corrections from fits to cumulants $M'_{n\geq 2}$ obtained from the moment data. Our conclusions are presented in Sec. VIII.

II. FORMALISM

A. Various moments of a distribution

The moments of a probability distribution function $p(k)$ are given by

$$M_n = \langle k^n \rangle = \int \mathrm{d}k\, p(k) k^n. \tag{4}$$

The characteristic function is the generator of these moments and is defined as the Fourier transform

$$\tilde{p}(y) = \langle e^{-iky} \rangle = \int \mathrm{d}k\, p(k) e^{-iky} = \sum_{n=0}^{\infty} \frac{(-iy)^n}{n!} M_n, \tag{5}$$

with $M_0 = 1$. The logarithm of $\tilde{p}(y)$ generates the cumulants (or connected moments) M'_n of the distribution

$$\ln \tilde{p}(y) = \sum_{n=1}^{\infty} \frac{(-iy)^n}{n!} M'_n, \tag{6}$$

and is called the cumulant generating function. For $n \geq 2$ the cumulants have the property of being invariant under shifts of the distribution. Replacing $p(k) \to p(k - k_0)$ takes $\tilde{p}(y) \to e^{-iyk_0} \tilde{p}(y)$, which shifts $M'_1 \to M'_1 + k_0$ while leaving all $M'_{n\geq 2}$ unchanged. Writing

[2] We thank C. Pahl for clarifying precisely how this was done.

[3] Another approach to hadronization corrections to moments of event shapes distributions based on renormalons is that of Gardi and Grunberg [45].

$$\sum_{N=0}^{\infty}\frac{(-iy)^N}{N!}M_N = \exp\Big[\sum_{j=1}^{\infty}\frac{(-iy)^j}{j!}M'_j\Big] = \prod_{j=1}^{\infty}\sum_{R=0}^{\infty}\frac{(-iy)^{jR}}{R!}\Big(\frac{M'_j}{j!}\Big)^R, \qquad (7)$$

one can derive an all-n relation between moments and cumulants of a distribution,

$$M_N = N!\sum_{i=1}^{p(N)}\prod_{j=1}^{N}\frac{(M'_j)^{\kappa_{ij}}}{\kappa_{ij}!(j!)^{\kappa_{ij}}}. \qquad (8)$$

Here the κ_{ij} are nonnegative integers which determine a partition of the integer N through $\sum_{j=1}^{N} j\kappa_{ij} = N$, and $p(N)$ is the number of unique partitions of N. [A partition of N is a set of integers which sum to N. Here κ_{ij} is the number of times the value j appears as a part in the ith partition, and corresponds to R in Eq. (7)]. As an example we quote the relation for $N = 4$ which has five partitions, $p(4) = 5$, giving

$$M_4 = M'_4 + 4M'_3M'_1 + 3M'^2_2 + 6M'_2M'^2_1 + M'^4_1. \qquad (9)$$

In the fourth partition, $i = 4$, we have $\kappa_{41} = 2$, $\kappa_{42} = 1$, and $\kappa_{43} = \kappa_{44} = 0$, and the factorials give the prefactor of 6. Equation (8) gives the moments M_i in terms of the cumulants M'_i, and these relations can be inverted to yield the formulas quoted for the cumulants in Eq. (3). $M'_2 \geq 0$ is the well-known variance of the distribution. Higher order cumulants can be positive or negative. The skewness of the distribution M'_3 provides a measure of its asymmetry, and we expect $M'_3 > 0$ for thrust with its long tail to the right of the peak. The kurtosis M'_4 provides a measure of the "peakedness" of the distribution, where $M'_4 > 0$ for a sharper peak than a Gaussian.[4]

The shift independence of the cumulants M'_n make them an ideal basis for studying event shape moments. In particular, since the leading $\mathcal{O}(\Lambda_{\rm QCD}/Q)$ power correction acts similar to a shift to the event shape distribution [36,43,50–52], we can anticipate that $M'_{n\geq 2}$ will be more sensitive to higher order power corrections. We will quantify this statement in the next section by using factorization for the thrust distribution to derive factorization formulas for the thrust cumulants in the form of an operator product expansion.

B. Thrust moments

We will first make use of the leading order factorization theorem, $\mathrm{d}\sigma/\mathrm{d}\tau = \int \mathrm{d}p(\mathrm{d}\hat\sigma/\mathrm{d}\tau)(\tau - p/Q)F_\tau(p)$, which is valid for all τ. It separates perturbative $\mathrm{d}\hat\sigma/\mathrm{d}\tau$ and nonperturbative $F_\tau(p)$ contributions to all orders in α_s and $\Lambda_{\rm QCD}/(Q\tau)$, but is only valid at leading order in $\Lambda_{\rm QCD}/Q$. For this factorization theorem we follow Ref. [8] (except that here we denote the nonperturbative soft function by F_τ).[5] We will then extend our analysis to parametrize corrections to all orders in $\Lambda_{\rm QCD}/Q$.

Taking moments of the leading order $\mathrm{d}\sigma/\mathrm{d}\tau$ gives[6]

$$\begin{aligned} M_n &= \int_0^{\tau_{\rm m}}\mathrm{d}\tau\tau^n\int_0^{Q\tau}\mathrm{d}p\,\frac{1}{\hat\sigma}\frac{\mathrm{d}\hat\sigma}{\mathrm{d}\tau}\Big(\tau - \frac{p}{Q}\Big)F_\tau(p) \\ &= \int_0^{\infty}\mathrm{d}\tau\mathrm{d}p\,\theta\Big(\tau_m - \tau - \frac{p}{Q}\Big)\Big(\tau + \frac{p}{Q}\Big)^n\frac{1}{\hat\sigma}\frac{\mathrm{d}\hat\sigma}{\mathrm{d}\tau}(\tau)F_\tau(p) \\ &= \Big[\sum_{\ell=0}^{n}\binom{n}{\ell}\Big(\frac{2}{Q}\Big)^{n-\ell}\hat M_\ell\Omega_{n-\ell}\Big] - E_n^{(A)} - E_n^{(B)}, \end{aligned} \qquad (10)$$

where $\hat\sigma$ is the perturbative total hadronic cross section and all hatted quantities are perturbative. In the last line of Eq. (10) we used $\theta(\tau_m - \tau - p/Q) = \theta(\tau_m - \tau)\times[1 - \theta(p/Q - \tau_m) - \theta(\tau_m - p/Q)\theta(p/Q + \tau - \tau_m)]$ to obtain the three terms. In Eq. (10) the term in square brackets is our desired result containing the perturbative $\hat M_n$ and nonperturbative Ω_n moments

$$\begin{aligned} \hat M_n &= \int_0^{\tau_{\rm m}}\mathrm{d}\tau\tau^n\frac{1}{\sigma}\frac{\mathrm{d}\hat\sigma}{\mathrm{d}\tau}(\tau), \qquad \hat M_0 = 1, \\ \Omega_n &= \int_0^{\infty}\mathrm{d}p\Big(\frac{p}{2}\Big)^nF_\tau(p), \qquad \Omega_0 = 1. \end{aligned} \qquad (11)$$

The small "error" terms in Eq. (10) are given by

$$\begin{aligned} E_n^{(A)} &= \sum_{\ell=0}^{n}\binom{n}{\ell}\Big(\frac{2}{Q}\Big)^{n-\ell}\hat M_\ell\int_{Q\tau_m}^{\infty}\mathrm{d}p\Big(\frac{p}{2}\Big)^{n-\ell}F_\tau(p), \\ E_n^{(B)} &= \int_0^{\tau_m}\mathrm{d}\tau\int_{Q(\tau_m-\tau)}^{Q\tau_m}\mathrm{d}p\Big(\tau + \frac{p}{Q}\Big)^n\frac{1}{\hat\sigma}\frac{\mathrm{d}\hat\sigma}{\mathrm{d}\tau}(\tau)F_\tau(p). \end{aligned} \qquad (12)$$

For the contribution $E_n^{(A)}$ the p integral is smaller than 10^{-30} for any Q for the first five moments, and hence $E_n^{(A)} \simeq 0$. This occurs because $F_\tau(p)$ falls off exponentially for $p \gtrsim 2\Omega_1 \sim 2\Lambda_{\rm QCD}$ [15,55], and hence values $p \geq Q\tau_m = Q/2$ are already far out on the exponential tail. The $E_n^{(B)}$ term gives a small contribution because the integral is suppressed by either F_τ or $\mathrm{d}\hat\sigma/\mathrm{d}\tau$: near the endpoint $\tau \sim \tau_m - 2\Lambda_{\rm QCD}/Q$ the p integration is not restricted and $F_\tau(p) \sim 1$, but $\mathrm{d}\hat\sigma/\mathrm{d}\tau$ is highly suppressed. For smaller τ the p integration is restricted and the exponential tail of $F_\tau(p)$ suppresses the contribution. We have checked numerically that at $Q = 91.2$ GeV [$Q = 35$ GeV], for the first moment the relative contribution of

[4]The cumulants of a Gaussian are all zero for $n > 2$, and the cumulants of a delta function are all zero for $n > 1$.

[5]Earlier discussions of shape functions for thrust can be found in Refs. [53,54].

[6]This manipulation is valid when the renormalization scales of the jet and soft function which implement resummation are $\mu_i = \mu_i(\tau - p/Q)$, rather than the more standard $\mu_i(\tau)$ used in Ref. [8]. Both choices are perturbatively valid, and we have checked that the difference is 0.4% for M_1, rising to 0.8% for M_5, and hence is always well within the perturbative uncertainty.

$E_1^{(B)}$ compared to the term in square brackets in Eq. (10) is $\mathcal{O}(10^{-7})[\mathcal{O}(10^{-6})]$, while for the fifth moment $E_5^{(B)}$ it is $\mathcal{O}(10^{-6})[\mathcal{O}(10^{-4})]$. This suppression does not rely on the model used for $F_\tau(p)$. Thus $E_n^{(B)}$ can also be safely neglected.

Within the theoretical precision we conclude that the leading factorization theorem for the distribution yields an operator product expansion that separates perturbative and nonperturbative corrections in the moments

$$M_n = \sum_{\ell=0}^{n} \binom{n}{\ell} \left(\frac{2}{Q}\right)^{n-\ell} \hat{M}_\ell \Omega_{n-\ell}. \tag{13}$$

For M_n the terms that numerically dominate are $\hat{M}_n$ and $\hat{M}_{n-1}\Omega_1/Q$. However for the cumulants M'_n there are cancellations, and Eq. (13) does not suffice due to our neglect so far of $(\Lambda_{\rm QCD}/Q)^j$ suppressed terms in the factorization expression for the thrust distribution.

To rectify this we parametrize the $(\Lambda_{\rm QCD}/Q)^j$ power corrections by a series of power-suppressed nonperturbative soft functions, $\Lambda^{j-1}F_{\tau,j}(p/\Lambda) \sim \Lambda_{\rm QCD}^{j-1}$. Here $\Lambda^{-1}F_{\tau,0}(p/\Lambda) = F_\tau(p)$ is the leading soft function from Eq. (10). We introduced the parameter $\Lambda = 400$ MeV $\sim \Lambda_{\rm QCD}$ to track the dimension of these subleading soft functions. This parametrization is motivated by the fact that subleading factorization results can in principle be derived with soft-collinear effective theory [56], and at each order in the power expansion will yield new soft function matrix elements.

Both the factorization analysis and calculation of cumulants is simpler in Fourier space, so we let

$$\begin{aligned} \sigma(y) &\equiv \int {\rm d}\tau e^{-iy\tau} \frac{{\rm d}\sigma}{{\rm d}\tau}(\tau), \\ F_{\tau,j}(z\Lambda) &\equiv \int \frac{{\rm d}p}{\Lambda} e^{-izp} F_{\tau,j}\left(\frac{p}{\Lambda}\right), \end{aligned} \tag{14}$$

and likewise for the leading power partonic cross section ${\rm d}\hat{\sigma}/{\rm d}\tau(\tau) \to \hat{\sigma}_0(y)$. The factorization-based formula for thrust is then

$$\frac{1}{\sigma}\sigma(y) = \frac{1}{\hat{\sigma}} \sum_{j=0}^{\infty} \left(\frac{\Lambda}{Q}\right)^j \hat{\sigma}_j(y) F_{\tau,j}\left(\frac{y\Lambda}{Q}\right), \tag{15}$$

where $\hat{\sigma}_{j>0}(y)$ accounts for perturbative corrections in the $(\Lambda_{\rm QCD}/Q)^j$ power correction. The $j = 0$ term is equivalent to the result used in Eq. (10), $F_\tau(p) = \Lambda F_{\tau,0}(p/\Lambda)$, and the normalization condition for the leading nonperturbative soft function is $F_{\tau,0}(z = 0) = 1$. The terms in Eq. (15) beyond $j = 0$ are schematic since in reality they may involve convolutions in more variables in the nonperturbative soft functions (as observed in the subleading $b \to s\gamma$ factorization theorem results [56–61]). Nevertheless the scaling is correct, and Eq. (15) will suffice for our analysis where we only seek to classify how various power corrections could enter higher moments or cumulants.

The identities $\sigma(y = 0)/\sigma = 1$ and $\hat{\sigma}_0(y = 0)/\hat{\sigma} = 1$ together with Eq. (15) imply

$$F_{\tau,j}(y = 0) = 0, \quad \text{for } j \geq 1. \tag{16}$$

Using the Fourier-space cross section the moments are

$$\begin{aligned} M_n &= i^n \frac{{\rm d}^n}{{\rm d}y^n}\left[\frac{1}{\sigma}\sigma(y)\right]_{y=0} \\ &= i^n \frac{{\rm d}^n}{{\rm d}y^n}\left[\frac{1}{\hat{\sigma}}\sum_{j=0}^{\infty} \hat{\sigma}_j(y)\left(\frac{\Lambda}{Q}\right)^j F_{\tau,j}\left(\frac{y\Lambda}{Q}\right)\right]_{y=0} \\ &= \sum_{j=0}^{\infty}\left(\frac{1}{Q}\right)^j \sum_{\ell=0}^{n}\binom{n}{\ell}\hat{M}_{n-\ell,j}\left(\frac{2}{Q}\right)^\ell \Omega_{\ell,j}, \end{aligned} \tag{17}$$

which extends the OPE in Eq. (13) to parametrize the $(\Lambda_{\rm QCD}/Q)^j$ power corrections. Here the perturbative and nonperturbative moments are defined as

$$\begin{aligned} \hat{M}_{n,j} &= i^n \frac{{\rm d}^n}{{\rm d}y^n}\left[\frac{1}{\hat{\sigma}}\hat{\sigma}_j(y)\right]_{y=0}, \\ \Omega_{n,j} &= \frac{i^n}{2^n}\frac{{\rm d}^n}{{\rm d}z^n}[\Lambda^j F_{\tau,j}(z\Lambda)]_{z=0}, \end{aligned} \tag{18}$$

where $\hat{M}_{n,j}$ is a dimensionless series in $\alpha_s(\mu)$ and $\Omega_{n,j} \sim \Lambda_{\rm QCD}^{n+j}$. In order for $\hat{M}_{n,j}$ to exist it is crucial that our $\hat{\sigma}_j(y)$ and its derivatives do not contain $\ln(y)$ dependence in the $y \to 0$ limit at any order in α_s. In τ space the perturbative coefficients have support over a finite range, $\tau \in [0, 1/2]$, and

$$\hat{\sigma}_j(y) = \int_0^{1/2} {\rm d}\tau e^{-i\tau y}\hat{\sigma}_j(\tau). \tag{19}$$

Therefore the existence of $\int_0^{1/2}{\rm d}\tau\hat{\sigma}_j(\tau)$ implies a well-defined Taylor series in y under the integrand in Eq. (19), and hence the existence of $\hat{M}_{n,j}$. This integral is the total perturbative cross section for $j = 0$. From Eq. (16) we have $\Omega_{0,j>0} = 0$, and furthermore $\Omega_{n,0} = \Omega_n$ and $\hat{M}_{n,0} = \hat{M}_n$.

For the first moment, Eq. (17) yields

$$M_1 = \hat{M}_1 + \frac{2\Omega_1}{Q} + \sum_{j=0}^{\infty} \hat{M}_{0,1+j}\frac{2\Omega_{1,1+j}}{Q^{2+j}}, \tag{20}$$

where the first two terms are determined by the leading order factorization theorem, while the last term identifies the scaling of contributions from $(\Lambda_{\rm QCD}/Q)^{2+j}$ power corrections. Two properties of Eq. (20) will be relevant for our analysis: first, there is no perturbative Wilson coefficient for the leading $2\Omega_1/Q$ power correction; and second, terms from beyond the leading factorization theorem only enter at $\mathcal{O}(\Lambda_{\rm QCD}^2/Q^2)$ and beyond. For higher order moments, $n \geq 2$, we have

$$M_n = \hat{M}_n + \frac{2n\Omega_1}{Q}\hat{M}_{n-1} + \frac{n(n-1)\Omega_2}{Q^2}\hat{M}_{n-2} + \frac{2n\Omega_{1,1}}{Q^2}\hat{M}_{n-1,1} + \mathcal{O}\Big(\frac{1}{Q^3}\Big). \tag{21}$$

Next we derive an analogous expression for the nth order cumulants for $n \geq 2$, which are generated from Fourier space by

$$M'_n = i^n \frac{\mathrm{d}^n}{\mathrm{d}y^n}\Big[\ln\frac{\sigma(y)}{\sigma}\Big]_{y=0}. \tag{22}$$

Equation (15) can be conveniently written as the product of three terms

$$\frac{1}{\sigma}\sigma(y) = \frac{1}{\hat{\sigma}}\hat{\sigma}_0(y) \times F_{\tau,0}\Big(\frac{y\Lambda}{Q}\Big) \times \Big[1 + \sum_{j=1}^{\infty}\bar{\sigma}_j(y)\Big(\frac{\Lambda}{Q}\Big)^j \bar{F}_{\tau,j}\Big(\frac{y\Lambda}{Q}\Big)\Big], \tag{23}$$

where bars indicate the ratios

$$\bar{\sigma}_j(y) = \frac{\hat{\sigma}_j(y)}{\hat{\sigma}_0(y)}, \qquad \bar{F}_{\tau,j}(x) = \frac{F_{\tau,j}(x)}{F_{\tau,0}(x)}. \tag{24}$$

From Eq. (16) we have $\bar{F}_{\tau,j}(x=0) = 0$ for all $j \geq 1$. Taking the logarithm of Eq. (23) expresses the thrust cumulants by the sum of three terms

$$M'_n = \hat{M}'_n + \Big(\frac{2}{Q}\Big)^n \Omega'_n + i^n \frac{\mathrm{d}^n}{\mathrm{d}y^n}\sum_{k=1}^{\infty}\frac{(-1)^{k+1}}{k} \times \Big[\sum_{j=1}^{\infty}\bar{\sigma}_j(y)\Big(\frac{\Lambda}{Q}\Big)^j \bar{F}_{\tau,j}\Big(\frac{y\Lambda}{Q}\Big)\Big]^k\Big|_{y=0}. \tag{25}$$

The first two terms involve the perturbative cumulants $\hat{M}'_n$ and the cumulants of the leading nonperturbative soft functions Ω'_n,

$$\hat{M}'_n = i^n \frac{\mathrm{d}^n}{\mathrm{d}y^n}\Big[\ln\frac{1}{\sigma}\hat{\sigma}_0(y)\Big]_{y=0}, \qquad \Omega'_n = \frac{i^n}{2^n}\frac{\mathrm{d}^n}{\mathrm{d}z^n}[\ln F_{\tau,0}(z\Lambda)]_{z=0}. \tag{26}$$

The third term in Eq. (25) represents contributions from power-suppressed terms that are not contained in the leading thrust factorization theorem. These terms start at $\mathcal{O}(\Lambda_{\rm QCD}^2/Q^2)$. At this order only $\bar{F}_{\tau,1}$ has to be considered. The terms $\bar{F}_{\tau,i>2}$ do not contribute due to explicit powers of $\Lambda_{\rm QCD}/Q$. Concerning $\bar{F}_{\tau,2}$, it must be hit by at least one derivative because $\bar{F}_{\tau,2}(0) = 0$, and hence does not contribute as well. Performing the nth derivative at $y = 0$ and keeping only the dominant term from the power corrections gives the OPE

$$M'_n = \hat{M}'_n + \frac{2^n\Omega'_n}{Q^n} + n\bar{M}_{n-1,1}\frac{2\Omega_{1,1}}{Q^2} + \mathcal{O}\Big(\frac{\Lambda_{\rm QCD}^3}{Q^3}\Big). \tag{27}$$

Here $\Omega_{1,1}$ is defined in Eq. (18). The perturbative coefficient is

$$\bar{M}_{j,1} = \Big[i^j \frac{\mathrm{d}^j}{\mathrm{d}y^j}\bar{\sigma}_1(y)\Big]_{y=0} \tag{28}$$

and so far unknown. For $n = 2$ the absence of a $1/Q$ power correction in Eq. (27) was discussed in Ref. [54].

The majority of our analysis will focus on M_1 where terms beyond the leading order factorization theorem are power suppressed. For our analysis of $M_{n\geq 2}$ we consider the impact of both $\alpha_s\Omega_1/Q$ corrections, and power corrections suppressed by more powers of $1/Q$. When we analyze $M'_{n\geq 2}$ we will consider both $1/Q^n$ and $1/Q^2$ power corrections in the fits.

III. RESULTS FOR M_1

In this section, we present the main results of our analysis, the fits to the first moment of the thrust distribution and the determination of $\alpha_s(m_Z)$ and Ω_1. Prior to presenting our final numbers in Sec. III D, we discuss various aspects important for their interpretation. In Sec. III A, we discuss the role of the log resummation contained in our fit code, the perturbative convergence for different kinds of expansion methods, and we illustrate the numerical impact of power corrections and the renormalon subtraction. We also briefly discuss the degeneracy between $\alpha_s(m_Z)$ and Ω_1 that motivates carrying out global fits to data covering a large range of Q values. In Sec. III B, we present the outcome of the theory parameter scans, on which the estimate of theory uncertainties in our fits are based, and show the final results. We also display results for the fits at various levels of accuracy. Section III C briefly discusses the effects of QED and bottom mass corrections. Section IV shows the results of a fit in which renormalon subtractions and power corrections are included, but resummation of logs in the thrust distribution is turned off.

For our moment analysis we use the thrust distribution code developed in Ref. [8], where a detailed description of the various ingredients may be found. We are able to perform fits with different levels of accuracy: fixed order at $\mathcal{O}(\alpha_s^3)$, resummation of large logarithms to N^{3}LL accuracy,[7] power corrections, and subtraction of the leading renormalon ambiguity. Recently the complete calculation of the $\mathcal{O}(\alpha_s^2)$ hemisphere soft function has become available [62–64], so the code is updated to use the fixed parameter $s_2 = -40.6804$ from Refs. [62,64]. A feature of our code is its ability to describe the thrust distribution in the whole range of thrust values. This is achieved with the introduction of what we call profile functions, which are τ-dependent factorization scales. In the e^+e^- annihilation process there are three relevant scales: hard, jet and soft, associated to the center of mass energy, the jet mass and the energy of soft radiation, respectively. The purpose of τ-dependent profile functions for these scales is to

[7] Throughout this publication N^{n}LL corresponds to the same order counting as N^{n}LL$'$ in Ref. [8].

smoothly interpolate between the peak region where we must ensure that $\mu_i > \Lambda_{\rm QCD}$, the dijet region where the summation of large logs is crucial, and the multijet region where regular perturbation theory is appropriate to describe the partonic contribution [8]. The major part of the higher order perturbative uncertainties are directly related to the arbitrariness of the profile functions, and are estimated by scanning the space of parameters that specify them. For details on the profile functions and the parameter scans we refer the reader to the Appendix. We note that our distribution code was designed for Q values above 22 GeV.

A. Ingredients

The theoretical fixed order expression for the thrust moments contain no large logarithms, so we might not expect that the resummation of logarithms in the thrust spectrum will play a role in the numerical analysis. We will show that there is nevertheless some benefit in accounting for the resummation of thrust logarithms. This is studied in Figs. 1 and 2, where for $Q = m_Z$ we compare the theoretical value of moments of the thrust distribution obtained in fixed order with those obtained including resummation. (The error bars for the fixed order expansion arise from varying the renormalization scale μ between $Q/2$ and $2Q$ and those for the resummed results arise from our theory parameter scan method).

In Fig. 1, we show the total hadronic cross section σ from the fixed order α_s expansion (blue points with small uncertainties sitting on the horizontal line) and determined from the integral over the log-resummed distribution with/without renormalon subtractions (red triangles and green squares). Both expansions are displayed including fixed order corrections up to order $\alpha_s(m_Z)$, $\alpha_s^2(m_Z)$ and $\alpha_s^3(m_Z)$, as indicated by the orders 1, 2, 3, respectively. We immediately notice that the resummed result is not as effective in reproducing the total cross section as the fixed order expansion. Predictions that sum large logarithms have a substantial (perturbative) normalization uncertainty. On the other hand, as shown in Ref. [8], the resummation of logarithms combined with the profile function approach leads to a description of the thrust spectrum that converges nicely over the whole physical τ range when the norm of the spectrum is divided out, a property not present in the spectrum of the fixed order expansion.

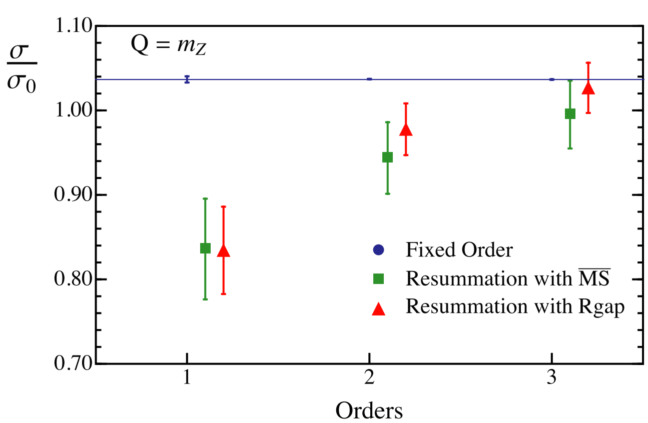

FIG. 1 (color online). Theoretical computations at various orders in perturbation theory for the total hadronic cross section at the Z pole normalized to the Born-level cross section σ_0. Here the small blue points correspond to fixed order perturbation theory, green squares to resummation without renormalon subtractions, and red triangles to resummation with renormalon subtractions.

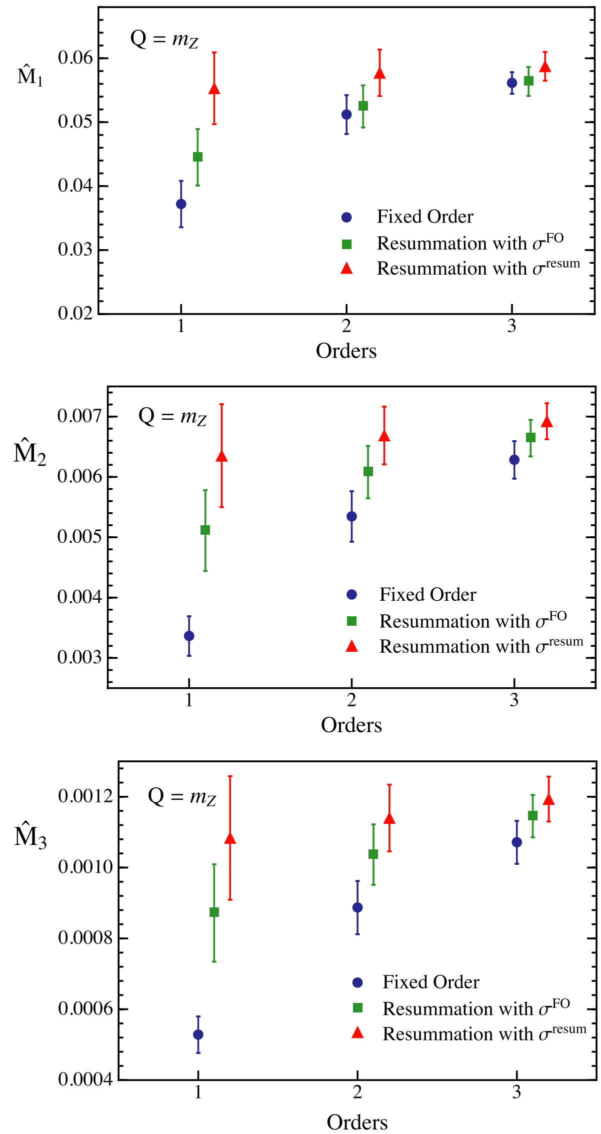

FIG. 2 (color online). Theoretical prediction for the first three moments at the Z pole at various orders in perturbation theory. The blue circles correspond to fixed order perturbation theory (normalized with the total hadronic cross section) at $\mathcal{O}(\alpha_s)$, $\mathcal{O}(\alpha_s^2)$ and $\mathcal{O}(\alpha_s^3)$, green squares correspond to resummed predictions at NLL, NNLL, and N^{3}LL normalized with the total hadronic cross section, and red triangles correspond to resummation normalized with the norm of the resummed distribution. For these plots we use $\alpha_s(m_Z) = 0.114$.

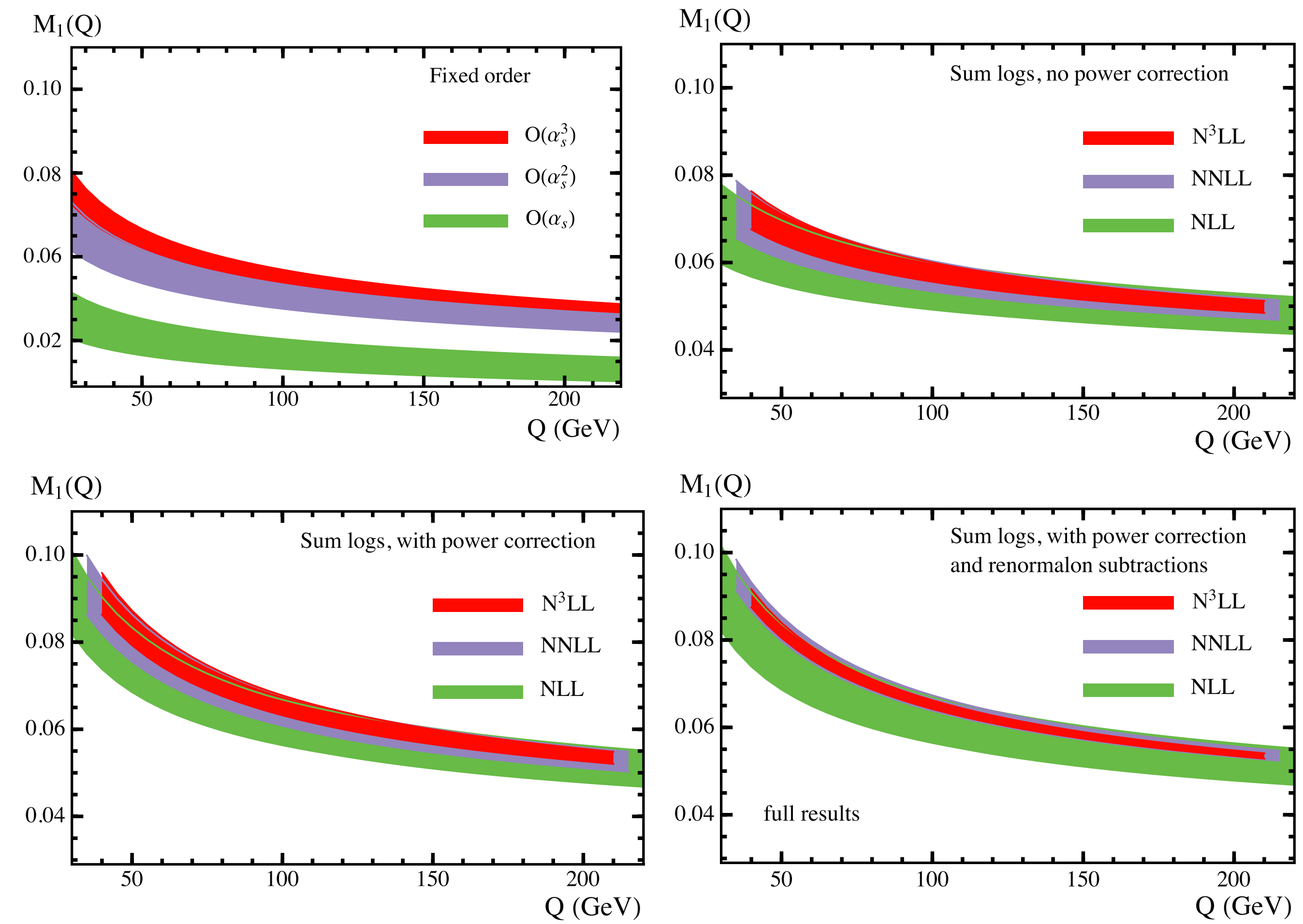

FIG. 3 (color online). Theory scan for uncertainties in pure QCD with massless quarks. The panels are fixed order (top-left), resummation without the nonperturbative correction (top-right), resummation with a nonperturbative function using the $\overline{\mathrm{MS}}$ scheme for $\bar{\Omega}_1$ (bottom-left), resummation with renormalon subtraction and a nonperturbative function in the Rgap scheme for Ω_1 (bottom-right).

In Fig. 2, the expansions of the partonic moments $\hat{M}_1$, $\hat{M}_2$, and $\hat{M}_3$ are displayed in the fixed order expansion (blue circles) and the log-resummed result with either the fixed order normalization (green squares) or a properly normalized spectrum (red triangles). We observe that the fixed order expansion has rather small variations from scale variation, but shows poor convergence indicating that its renormalization scale variation underestimates the perturbative uncertainty. For $\hat{M}_1$ the fixed order and log-resummed expressions with a common fixed-order normalization (blue circles and green squares) agree well at each order, indicating that, as expected, large logarithms do not play a significant role for this moment. On the other hand, the expansion based on the properly normalized log-resummed spectrum exhibits excellent convergence, and also has larger perturbative uncertainties at the lowest order. In particular, for the red triangles the higher order results are always within the 1-σ uncertainties of the previous order. The result shows that using the normalized log-resummed spectrum for thrust, which converges nicely for all τ, also leads to better convergence properties of the moments. At third order all the fixed order and resummed partonic moments are consistent with each other. Since the log-resummed moments exhibit more realistic estimates of perturbative uncertainties at each order, we will use the normalized resummed moments for our fit analysis.[8]

In Fig. 3, we show how the inclusion of various ingredients (fixed order contributions, log resummation, power corrections, renormalon subtraction) affects the convergence and uncertainty of our theoretical prediction for the first moment of the thrust distribution as a function of Q. From these plots we can observe four points: (i) Fixed order perturbation theory does not converge very well.

[8]At N^{3}LL in our most complete theory set up the norm of the distribution and total hadronic cross section are fully compatible within uncertainties, so it does not matter which is used. Following Ref. [8], at N^{3}LL we choose to normalize the distribution with the fixed-order total hadronic cross section since it is faster.

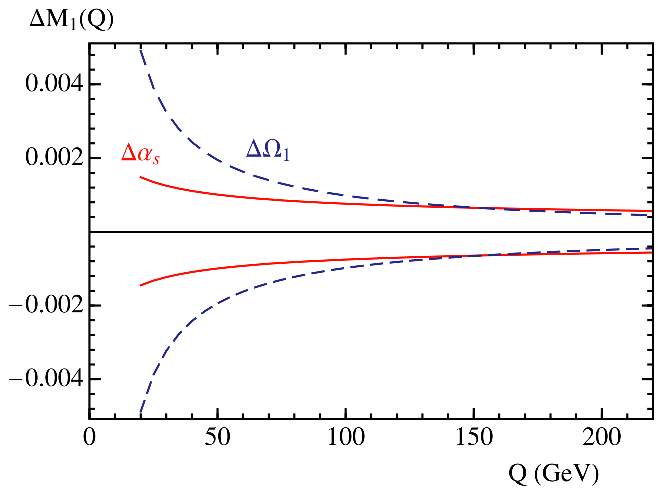

FIG. 4 (color online). Difference between theoretical predictions with default parameters for the first moment as a function of Q when varying one parameter at a time. The red solid line corresponds to varying $\Delta\alpha_s(m_Z) = \pm 0.001$ and the blue dashed lines to varying $\Delta\Omega_1 = \pm 0.1$, with respect to the pure QCD best-fit values. There is a strong degeneracy of the two parameters in the region $Q > 100$ GeV, which is obviously broken when considering values of Q below 70 GeV.

(ii) Resummation of large logarithms in the distribution, when normalized with the integral of the resummed distribution, improves convergence for every center of mass energy. (iii) The inclusion of power corrections has the effect of a $1/Q$-modulated vertical shift on the value of the first moment. (iv) The subtraction of the renormalon ambiguity reduces the theoretical uncertainty. This picture for the first moment is consistent with the results of Ref. [8] for the thrust distribution.

Another important element of our analysis is that we perform global fits, simultaneously using data at a wide range of center of mass energies Q. This is motivated by the fact that for each Q there is a complete degeneracy between changing $\alpha_s(m_Z)$ and changing Ω_1, which can be lifted only through a global analysis. Figure 4 shows the difference between the theoretical prediction of M_1 as a function of Q, when $\alpha_s(m_Z)$ or Ω_1 are varied by ± 0.001 and ± 0.1 GeV, respectively. We see that the effect of a variation in $\alpha_s(m_Z)$ can be compensated with an appropriate variation in Ω_1 at a given center of mass energy (or in a small Q range). This degeneracy is broken if we perform a global fit including the wide range of Q values shown in the figure.

Finally, in Fig. 5 we show $\alpha_s(m_Z)$ extracted from fits to the first moment of the thrust distribution at three-loop accuracy including sequentially the different effects our code has implemented: $\mathrm{O}(\alpha_s^3)$ fixed order, N³LL resummation, power corrections, renormalon subtraction, b-quark mass and QED. The error bars of the first two points at the left-hand side do not contain an estimate of uncertainties associated with the power correction. Though smaller, the resummed result is compatible at the 1-σ level with the fixed order result. The inclusion of the power correction is the element which has the greatest impact on $\alpha_s(m_Z)$; for the $\overline{\mathrm{MS}}$ definition of Ω_1 it reduces the central value by 7%. The subtraction of the renormalon ambiguity in the Rgap scheme reduces the theoretical uncertainty by a factor of 3, while b-quark mass and QED effects give negligible contributions with current uncertainties.

B. Uncertainty analysis

In Fig. 6, we show the result of our theory scan to determine the perturbative uncertainties. At each order we carried out 500 fits, with theory parameters randomly

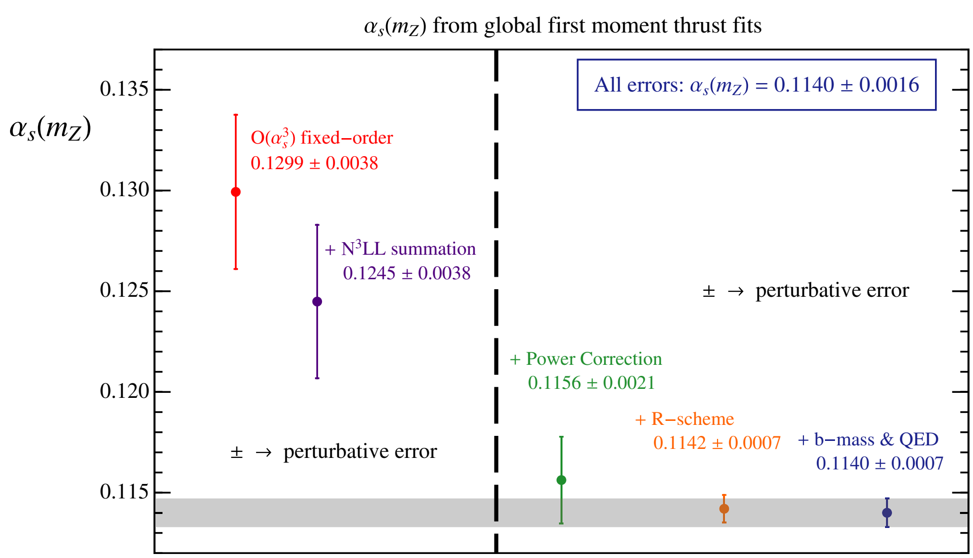

FIG. 5 (color online). Evolution of the best-fit values for $\alpha_s(m_Z)$ from thrust first moment fits when including various levels of improvement with respect to fixed order QCD. Only points at the right of the vertical dashed line include nonperturbative effects.

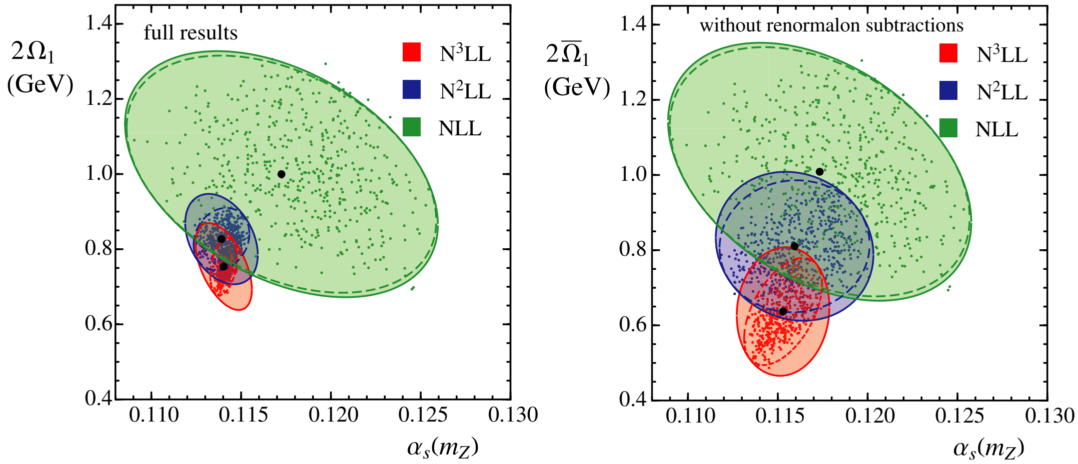

FIG. 6 (color online). Distribution of best-fit points in the $\alpha_s(m_Z)$-$2\Omega_1$ and $\alpha_s(m_Z)$-$2\bar{\Omega}_1$ planes. The left panel shows results including perturbation theory, resummation of the logs, the soft nonperturbative function, and Ω_1 defined in the Rgap scheme with renormalon subtractions. The right panel shows the same results, but with $\bar{\Omega}_1$ defined in the $\overline{\rm MS}$ scheme, and without renormalon subtractions. In both panels the dashed lines correspond to an ellipse fit to the contour of the best-fit points to determine the theoretical uncertainty. The respective total (experimental + theoretical) 39% C.L. standard error ellipses are displayed (solid lines), which correspond to 1-σ (68% C.L.) for either one-dimensional projection.

chosen in the ranges given in Table VIII of the Appendix (where further details may be found). The left panel of Fig. 6 shows results with renormalon subtractions using the Rgap scheme for Ω_1, and the right panel shows results in the $\overline{\rm MS}$ scheme without renormalon subtractions. Each point in the plot represents the result of a single fit. As described in the Appendix, in order to estimate perturbative uncertainties, we fit an ellipse to the contour of best-fit points in the α_s-$2\Omega_1$ plane, and we interpret this as 1-σ theoretical error ellipse. This is represented by the dashed lines in Fig. 6. The solid lines represent the combined (theoretical and experimental) standard error ellipses. These are obtained by adding the theoretical and experimental error matrices which determined the individual ellipses. The central values of the fits, collected in Tables I and II, are determined from the average of the maximal and minimal values of the theory scan, and are very close to the central values obtained when running with our default parameters. The minimal χ^2 values for these fits are quoted in Table III as well. The best fit based on our full code has $\chi^2/\text{d.o.f.} = 1.325 \pm 0.002$ where the range incorporates the variation from the displayed scan points at N^{3}LL. The fit results show a substantial reduction of the theoretical uncertainties with increasing perturbative order. Removal of the $\mathcal{O}(\Lambda_{\rm QCD})$ renormalon improves the perturbative convergence and leads to a reduction of the theoretical uncertainties at the highest order by a factor of 2 in Ω_1, and factor of 3 in $\alpha_s(m_Z)$

To analyze in detail the experimental and the total uncertainties of our results, we refer now to Fig. 7. Here we show the error ellipses for our highest order fit, which includes resummation, power corrections, renormalon subtraction, QED and b-quark mass contributions. The green dotted, blue dashed, and the solid red lines represent the standard error ellipses for, respectively, experimental, theoretical, and combined theoretical and experimental uncertainties. The experimental and theory error ellipses are defined by $\Delta\chi^2 = 1$ since we are most interested in the one-dimensional projection onto α_s. The correlation

TABLE I. Central values for $\alpha_s(m_Z)$ at various orders with theory uncertainties from the parameter scan (first value in parentheses), and experimental and hadronic error added in quadrature (second value in parentheses). The bold N^{3}LL value is our final result, while values below it show the effect of leaving out the QED and b-mass corrections.

Order	$\alpha_s(m_Z)$ (with $\bar{\Omega}_1^{\overline{\rm MS}}$)	$\alpha_s(m_Z)$ (with $\Omega_1^{\rm Rgap}$)
NLL	0.1173(82)(13)	0.1172(82)(13)
NNLL	0.1159(41)(14)	0.1139(15)(13)
N^{3}LL (full)	0.1153(21)(14)	**0.1140(07)(14)**
N^{3}LL$_{({\rm QCD}+m_b)}$	0.1160(20)(14)	0.1146(07)(14)
N^{3}LL$_{(\text{pure QCD})}$	0.1156(21)(14)	0.1142(07)(14)

TABLE II. Central values for Ω_1 at the reference scales $R_\Delta = \mu_\Delta = 2$ GeV and for $\bar{\Omega}_1$ and at various orders. The parentheses show theory uncertainties from the parameter scan, and experimental and hadronic uncertainty added in quadrature, respectively. The bold value is our final result, while the N^{3}LL values below it show the effect of leaving out the QED and b-mass corrections.

Order	$\bar{\Omega}_1$ ($\overline{\rm MS}$) [GeV]	Ω_1 (Rgap) [GeV]
NLL	0.504(157)(45)	0.500(153)(45)
NNLL	0.405(82)(47)	0.413(43)(44)
N^{3}LL(full)	0.318(75)(49)	**0.377(39)(44)**
N^{3}LL$_{({\rm QCD}+m_b)}$	0.310(74)(49)	0.369(34)(44)
N^{3}LL$_{(\text{pure QCD})}$	0.350(67)(49)	0.402(35)(44)

TABLE III. Comparison of first moment fit results for analyses with full results and $\Omega_1 = \Omega_1^{\mathrm{Rgap}}$, with $\bar{\Omega}_1$ and no renormalon subtractions, without power corrections, and at fixed order without power corrections or log resummation. The first number in parentheses corresponds to the theory uncertainty, whereas the second corresponds to the experimental and hadronic uncertainty added in quadrature for the first two rows, and experimental uncertainty for the last two rows.

	$\alpha_s(m_Z)$	$\chi^2/(\mathrm{dof})$
N^{3}LL with Ω_1^{Rgap}	0.1140(07)(14)	1.33
N^{3}LL with $\bar{\Omega}_1^{\overline{\mathrm{MS}}}$	0.1153(21)(14)	1.33
N^{3}LL no power corr.	0.1236(39)(03)	2.03
$\mathcal{O}(\alpha_s^3)$ fixed order no power corr.	0.1305(39)(04)	2.52

matrix of the experimental, theory, and total error ellipses are ($i, j = \alpha_s, 2\Omega_1$)

$$V_{ij} = \begin{pmatrix} \sigma_{\alpha_s}^2 & 2\sigma_{\alpha_s}\sigma_{\Omega_1}\rho_{\alpha\Omega} \\ 2\sigma_{\alpha_s}\sigma_{\Omega_1}\rho_{\alpha\Omega} & 4\sigma_{\Omega_1}^2 \end{pmatrix},$$
$$V_{ij}^{\mathrm{exp}} = \begin{pmatrix} 1.93(15)\times 10^{-6} & -1.18(13)\times 10^{-4}\,\mathrm{GeV} \\ -1.18(13)\times 10^{-4}\,\mathrm{GeV} & 0.79(13)\times 10^{-2}\,\mathrm{GeV}^2 \end{pmatrix},$$
$$V_{ij}^{\mathrm{theo}} = \begin{pmatrix} 5.56\times 10^{-7} & 1.85\times 10^{-5}\,\mathrm{GeV} \\ 1.85\times 10^{-5}\,\mathrm{GeV} & 5.82\times 10^{-3}\,\mathrm{GeV}^2 \end{pmatrix},$$
$$V_{ij}^{\mathrm{tot}} = \begin{pmatrix} 2.49(15)\times 10^{-6} & -0.99(13)\times 10^{-4}\,\mathrm{GeV} \\ -0.99(13)\times 10^{-4}\,\mathrm{GeV} & 1.37(13)\times 10^{-2}\,\mathrm{GeV}^2 \end{pmatrix}, \tag{29}$$

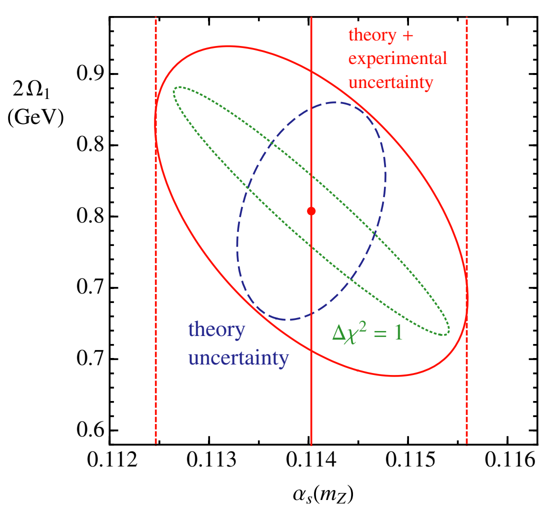

FIG. 7 (color online). Experimental $\Delta\chi^2 = 1$ standard error ellipse (dotted green) at N^{3}LL accuracy with renormalon subtractions, in the α_s-$2\Omega_1$ plane. The dashed blue ellipse represents the theory uncertainty which is obtained by fitting an ellipse to the contour of the distribution of the best-fit points. This ellipse should be interpreted as the 1-σ theory uncertainty for 1 parameter (39% confidence for 2 parameters). The solid red ellipse represents the total (combined experimental and perturbative) uncertainty ellipse.

where the experimental correlation coefficient is significant and reads

$$\rho_{\alpha\Omega}^{\mathrm{exp}} = -0.96(14). \tag{30}$$

Adding the theory scan uncertainties reduces the correlation coefficient in Eq. (30) to

$$\rho_{\alpha\Omega}^{\mathrm{total}} = -0.54(8). \tag{31}$$

In both Eqs. (30) and (31), the numbers in parentheses capture the range of values obtained from the theory scan. From V_{ij}^{exp} in Eq. (29) it is possible to extract the experimental uncertainty for α_s and Ω_1 and the uncertainty due to variations of Ω_1 and α_s, respectively,

$$\begin{aligned} \sigma_{\alpha_s}^{\mathrm{exp}} &= \sigma_{\alpha_s}\sqrt{1-\rho_{\alpha\Omega}^2} = 0.0004, \\ \sigma_{\Omega_1}^{\mathrm{exp}} &= \sigma_{\Omega_1}\sqrt{1-\rho_{\alpha\Omega}^2} = 0.013\ \mathrm{GeV}, \\ \sigma_{\alpha_s}^{\Omega_1} &= \sigma_{\alpha_s}|\rho_{\alpha\Omega}| = 0.0014, \\ \sigma_{\Omega_1}^{\alpha_s} &= \sigma_{\Omega_1}|\rho_{\alpha\Omega}| = 0.044\ \mathrm{GeV}. \end{aligned} \tag{32}$$

Figure 7 shows the total uncertainty in our final result quoted in Eq. (34) below.

The correlation exhibited by the green dotted experimental error ellipse in Fig. 7 is given by the line describing the semimajor axis

$$\frac{\Omega_1}{32.82\ \mathrm{GeV}} = 0.1255 - \alpha_s(m_Z). \tag{33}$$

Note that extrapolating this correlation to the extreme case where we neglect the nonperturbative corrections ($\Omega_1 = 0$) gives $\alpha_s(m_Z) \to 0.1255$.

C. Effects of QED and the *b* mass

The experimental correction procedures applied to the AMY, JADE, SLC, DELPHI and OPAL data sets were typically designed to eliminate initial state photon radiation, while those of the TASSO, L3 and ALEPH Collaborations eliminated initial and final state photon radiation. It is straightforward to test for the effect of these differences in the fits by using our theory code with QED effects turned on or off depending on the data set. Using our N^{3}LL order code in the Rgap scheme we obtain the central values $\alpha_s(m_Z) = 0.1143$ and $\Omega_1 = 0.376$ GeV. Comparing to our default results given in Tables I and II, which are based on the theory code were QED effects are included for all data sets, we see that the central value for α_s is larger by 0.0003 and the one for Ω_1 is smaller by 0.001 GeV. This shift is substantially smaller than our perturbative uncertainty. Hence our choice to use the theory code with QED effects included everywhere as the default for our analysis does not cause an observable bias regarding experiments which remove final state photons.

By comparing the N^{3}LL (pure massless QCD) and N^{3}LL (QCD + m_b) entries in Tables I and II, we see that including finite b-mass corrections causes a very mild shift of $\simeq +0.0004$ to $\alpha_s(m_Z)$, and a somewhat larger shift of $\simeq -0.033$ GeV to Ω_1. In both cases these shifts are within the 1-σ theory uncertainties. In the N^{3}LL (pure massless QCD) analysis the b-quark is treated as a massless flavor, hence this analysis differs from that done by JADE [23] where primary b quarks were removed using Monte Carlo generators.

D. Final results

As our final result for $\alpha_s(m_Z)$ and Ω_1, obtained at N^{3}LL order in the Rgap scheme for $\Omega_1(R_\Delta, \mu_\Delta)$, including bottom quark mass and QED corrections we obtain

$$\begin{aligned} \alpha_s(m_Z) &= 0.1140 \pm (0.0004)_{\rm exp} \pm (0.0013)_{\rm hadr} \\ &\quad \pm (0.0007)_{\rm pert}, \\ \Omega_1(R_\Delta, \mu_\Delta) &= 0.377 \pm (0.013)_{\rm exp} \pm (0.042)_{\alpha_s(m_Z)} \\ &\quad \pm (0.039)_{\rm pert}\ {\rm GeV}, \end{aligned} \tag{34}$$

where $R_\Delta = \mu_\Delta = 2$ GeV and we quote individual 1-σ uncertainties for each parameter. Here $\chi^2/\mathrm{d.o.f.} = 1.33$. Equation (34) is the main result of this work.

In Fig. 8, we show the first moment of the thrust distribution as a function of the center of mass energy Q, including QED and m_b corrections. We use here the best-fit values given in Eq. (34). The band displays the theoretical uncertainty and has been determined with a scan on the parameters included in our theory, as explained in the Appendix. The fit result is shown in comparison with data from ALEPH, OPAL, L3, DELPHI, JADE, AMY and TASSO. Good agreement is observed for all Q values.

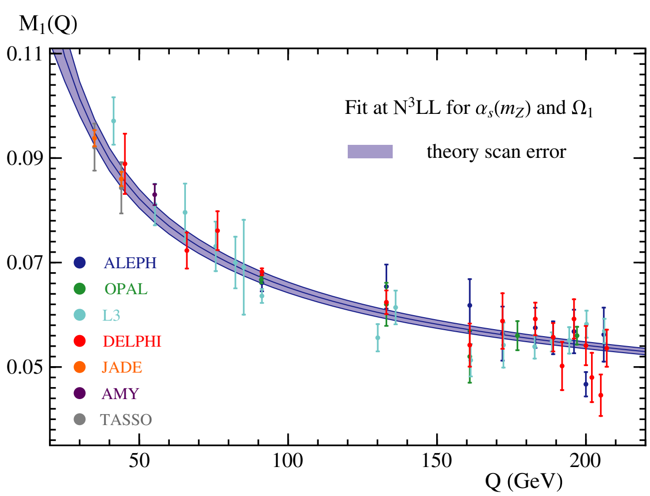

FIG. 8 (color online). First moment of the thrust distribution as a function of the center of mass energy Q, using the best-fit values for $\alpha_s(m_Z)$ and Ω_1 in the Rgap scheme as given in Eq. (34). The blue band represents the perturbative uncertainty determined by our theory scan. Data is from ALEPH, OPAL, L3, DELPHI, JADE, AMY and TASSO.

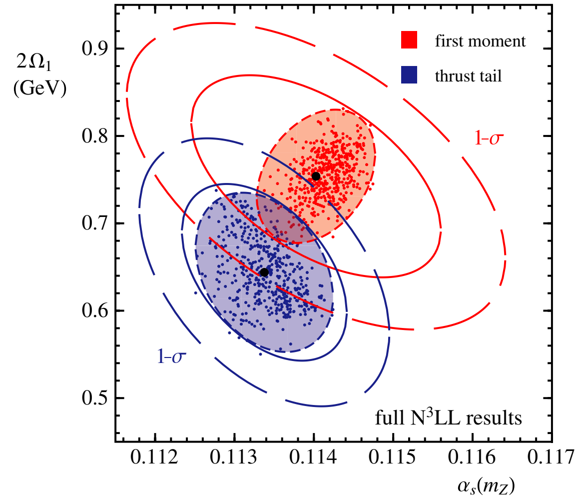

FIG. 9 (color online). Comparison of $\alpha_s(m_Z)$ and Ω_1 determinations from thrust first moment data (red upper right ellipses) and thrust tail data (blue lower left ellipses). The plot corresponds to fits with N^{3}LL accuracy and in the Rgap scheme. The tail fits are performed with our improved code which uses a new nonsingular two-loop function, and the now known two-loop soft function. Dashed lines correspond to theory uncertainties, solid lines correspond to $\Delta\chi^2 = 1$ combined theoretical and experimental error ellipses, and wide-dashed lines correspond to $\Delta\chi^2 = 2.3$ combined error ellipses (corresponding to 1-σ uncertainty in two dimensions).

It is interesting to compare the result of this analysis with the result of our earlier fit of thrust tail distributions in Ref. [8]. This is shown in Fig. 9. Here the red upper shaded area and corresponding ellipses show the results from fits to the first moment of the thrust distribution, while the blue lower shaded area and ellipses show the result from fits of its tail region. Both analyses show the theory (dashed lines) and combined theoretical and experimental (solid lines) standard error ellipses, as well as the ellipses which correspond to $\Delta\chi^2 = 2.3$ (68% C.L. for a two-parameter fit, wide-dashed lines). We see that the two analyses are compatible.

IV. FIXED ORDER ANALYSIS OF M_1

It is interesting to compare the result of our best fit with an analysis where we do not perform resummation in the thrust distribution, but where power corrections and renormalon subtractions are still considered. This is achieved by setting the scales μ_H, μ_S, μ_J, $\mu_{\rm ns}$ in our theoretical prediction all to a common scale $\mu \sim Q$. We use R for the scale of the renormalon subtractions and renormalization group evolved power correction. Finally we will neglect QED and b-mass corrections in this subsection. Up to the treatment of power corrections and perturbative subtractions, the fixed order results used for this analysis are thus equivalent to those used in Ref. [48].

The OPE formula for the first moment in the Rgap scheme for this situation is given by

$$M_1 = \hat{M}_1^{\rm Rgap}(R,\mu) + \frac{2\Omega_1(R,\mu)}{Q},$$
$$\Omega_1(R,\mu) = \Omega_1 + \bar{\Delta}(R,\mu) - \bar{\Delta}(R_\Delta,\mu_\Delta). \tag{35}$$

In Eq. (35), the Ω_1 with no arguments is the value determined by the fits, which is in the Rgap scheme at the reference scale $\mu_\Delta = R_\Delta = 2$ GeV. Here $\bar{\Delta}(R,\mu)$ is the running gap parameter, and $\bar{\Delta}(R,\mu) - \bar{\Delta}(R_\Delta,\mu_\Delta)$ is used to sum logarithms from (R_Δ,μ_Δ) to (R,μ) in Eq. (35). The analytic expression for $\bar{\Delta}(R,\mu) - \bar{\Delta}(R_\Delta,\mu_\Delta)$ can be found in Eq. (41) of Ref. [8] (see also Ref. [16]). The perturbative $\hat{M}_1^{\rm Rgap}$ is related to the perturbative $\overline{\rm MS}$ result by

$$\hat{M}_1^{\rm Rgap}(R,\mu) = \hat{M}_1^{\overline{\rm MS}}(\mu) + \frac{2\delta(R,\mu)}{Q},$$
$$\delta(R,\mu) = e^{\gamma_E} R \sum_{i=1}^{3} \alpha_s(\mu)^i \delta_i(R,\mu), \tag{36}$$

where the subtractions terms are [8,16]

$$\delta_1(R,\mu) = -0.848826 L_R,$$
$$\delta_2(R,\mu) = -0.156279 - 0.46663 L_R - 0.517864 L_R^2,$$
$$\delta_3(R,\mu) = -0.552986 - 0.622467 L_R - 0.777219 L_R^2 - 0.421261 L_R^3, \tag{37}$$

with $L_R = \ln(\mu/R)$. In Eq. (36) $\delta(R,\mu)$ cancels the $\mathcal{O}(\Lambda_{\rm QCD})$ renormalon in $\hat{M}_1^{\overline{\rm MS}}(\mu)$, and it is crucial that the coupling expansions in both of these objects are done at the same scale, $\alpha_s(\mu)$, for this cancellation to take place. The relation to the $\overline{\rm MS}$ scheme power correction is $\bar{\Omega}_1 = \Omega_1 + \delta(R_\Delta,\mu_\Delta)$, and the OPE in the $\overline{\rm MS}$ scheme at this level is

$$M_1 = \hat{M}_1^{\overline{\rm MS}}(\mu) + \frac{2\bar{\Omega}_1}{Q}. \tag{38}$$

In the $\overline{\rm MS}$ result there are no perturbative renormalon subtractions (and thus no log resummation related to the renormalon subtractions) and the parameter $\bar{\Omega}_1$ has a $\Lambda_{\rm QCD}$ renormalon ambiguity.

We will perform fits to the experimental data following the same procedure discussed in the previous section. Using Eq. (35) we consider two cases, (i) $R \sim Q$ where Ω_1 is renormalization group evolved to R and there are no large logarithms in the renormalon subtractions, and (ii) fixing R at the reference scale, $R = 2$ GeV, in which case large logarithms are present in the renormalon subtractions. We will also consider a third case, (iii), using the $\overline{\rm MS}$ OPE of Eq. (38). Results for these fits are shown in Tables IV and V. For all cases $\chi^2/{\rm d.o.f.} \simeq 1.32$.

For case (i) we take $R \sim \mu \sim Q$, so there are no large logarithms in the $\delta(R,\mu)$ of Eq. (35), and all large logarithms associated with renormalon subtractions are summed in $\bar{\Delta}(R,\mu) - \bar{\Delta}(R_\Delta,\mu_\Delta)$. Here we estimate the perturbative uncertainty in $\alpha_s(m_Z)$ and Ω_1 by varying the renormalization scale μ and the scale R independently in the range $\{2Q, Q/2\}$. We use one-half the maximum minus minimum variation as the uncertainty, and the average for the central value. The results for both $\alpha_s(m_Z)$ and Ω_1 are fully compatible at 1-σ to our final results shown in Eq. (34). The agreement is even closer to the central values for the fits without QED or b-mass corrections in Tables I and II, namely $\alpha_s(m_Z) = 0.1142(07)(14)$ and $\Omega_1 = 0.402(35)(44)$. The one difference is that the perturbative uncertainty for Ω_1 in Table V is a factor of 3 smaller. The case (i) results in the table also exhibit nice order-by-order convergence, and if one plots M_1 versus Q (analogous to Fig. 2) the uncertainty bands are entirely contained within one another. In order to be conservative, we take our resummation analysis in Eq. (34) as our final results (with its larger perturbative uncertainty and inclusion of QED and b-mass corrections).

For case (ii) we take $R \sim 2$ GeV and $\mu \sim Q$ as typical values, so there are large logarithms, $\ln(R/Q)$, in the $\delta(R,\mu)$ renormalon subtractions. The central value for $\alpha_s(m_Z)$ at $\mathcal{O}(\alpha_s^3)$ is again fully compatible with that in Eq. (34). Here we estimate the perturbative uncertainty in $\alpha_s(m_Z)$ by varying $\mu \in \{2Q, Q/2\}$ and $R = 2 \pm 1$ GeV. Due to the large logarithms the perturbative uncertainty in $\alpha_s(m_Z)$ for case (ii), shown in Table IV, is 3 times larger than for case (i). It is also compatible with the difference between central values at $\mathcal{O}(\alpha_s^2)$ and $\mathcal{O}(\alpha_s^3)$. To estimate the uncertainty for Ω_1 we only vary μ, which leads to the rather large error estimate for Ω_1 shown in Table V. The contrast between the precision of the results in case (i), to

TABLE IV. $\overline{\rm MS}$ scheme values for $\alpha_s(m_Z)$ obtained from various fixed order analyses. The first value in parentheses is the uncertainty from higher order perturbative corrections (obtained by the method described in the text), while the second value is the combined experimental and hadronization uncertainty.

Order	$\mathcal{O}(\alpha_s^2)$	$\mathcal{O}(\alpha_s^3)$
(i) Rgap R-RGE	0.1159(27)(14)	0.1146(06)(14)
(ii) Rgap FO Subt.	0.1185(63)(15)	0.1138(20)(14)
(iii) $\overline{\rm MS}$ for $\bar{\Omega}_1$	0.1278(124)(19)	0.1186(38)(14)

TABLE V. Ω_1 or $\bar{\Omega}_1$ values obtained from fixed order analyses at various orders. The first value in parentheses is the uncertainty from higher order perturbative corrections (obtained by the method described in the text), while the second value is the combined experimental and hadronization uncertainty.

Order	$\mathcal{O}(\alpha_s^2)$	$\mathcal{O}(\alpha_s^3)$
(i) Rgap R-RGE	0.407(8)(45)	0.400(8)(45)
(ii Rgap FO Subt.	0.216(126)(133)	0.359(42)(62)
(iii) $\overline{\rm MS}$ for $\bar{\Omega}_1$	0.388(62)(47)	0.350(54)(44)

the results in case (ii), illustrates the importance of summing large logarithms in the renormalon subtractions.

For case (iii), where the $\bar{\Omega}_1$ power correction is defined in $\overline{\rm MS}$ we do not have renormalon subtractions (and hence no large logs in subtractions). Due to the poor convergence of the fixed order prediction for the first moment, seen from the blue fixed order points in Fig. 2, it is not clear whether varying μ in the range $\{2Q, Q/2\}$ gives a realistic perturbative uncertainty estimate. Hence we determine the perturbative uncertainty for case (iii) in Tables IV and V by varying μ in the range $\{2Q, Q/2\}$ and multiply the result by a factor of 2. The perturbative uncertainties for $\alpha_s(m_Z)$ are a factor of 2 larger than in case (ii). The central values for $\alpha_s(m_Z)$ in case (iii) are also larger, but are compatible with those in case (ii) and Eq. (34) within 1-σ.

It is interesting to compare our results to those of Ref. [48], which also performs a fixed order analysis at $\mathcal{O}(\alpha_s^3)$, and incorporates subtractions based on the dispersive model.[9] Here the subtractions contain logarithms, $\ln(\mu_I/\mu)$, where $\mu_I \sim 2$ GeV and $\mu \sim Q$, that are not resummed. From a fit to M_1 in thrust they obtained $\alpha_s(m_Z) = 0.1166 \pm 0.0015_{\rm exp} \pm 0.0032_{\rm th}$ where the first uncertainty is experimental and the second is theoretical. Our corresponding result is the one in case (ii), and the central values and uncertainties for $\alpha_s(m_Z)$ are fully compatible. The perturbative uncertainty they obtain is a factor of 1.6 larger than ours. It arises from varying the renormalization scale $\mu \in \{2Q, Q/2\}$, the $\mathcal{O}(\alpha_s^2)$ Milan factor $\mathcal{M}$ by 20%, and the infrared scale $\mu_I = 2 \pm 1$ GeV in the dispersive model. In our analysis there is no precise analog of the Milan factor because our subtractions and Rgap scheme for Ω_1 fully account for two and three gluon infrared effects up to $\mathcal{O}(\alpha_s^3)$ that are associated to thrust. Other than this, the difference can be simply attributed to the differences in subtraction schemes which have an impact on the μ scale uncertainty. Finally, note that we have implemented the analytic results of Ref. [48] and confirmed their μ and μ_I uncertainties.

V. JADE DATA SETS

As discussed in Sec. I, our global data set includes thrust moment results from ALEPH, OPAL, L3, DELPHI, AMY, TASSO and the JADE data from Ref. [22]. In this section, we discuss the impact on the results in Secs. III and IV of replacing the JADE data from Ref. [22] with moment results from an updated analysis carried out in Ref. [23], which removes the contributions from primary $b\bar{b}$ pair production and provides in addition measurements at $Q = 14$ and 22 GeV. In Fig. 10, we show the data for M_1, including the JADE results from Refs. [22,23]. The most significant difference occurs at $Q = 44$ GeV. Our analysis will treat these data sets on the same footing without attempting to account for the effect of removing the $b\bar{b}$'s.

For our analysis here, with theory results at N^{3}LL + $\mathcal{O}(\alpha_s^3)$, we continue to exclude center of mass energies $Q \leq 22$ GeV as in Sec. III. The dependence of the global fit result on the data set for M_1 is shown in Fig. 11. Theoretical uncertainties are analyzed again by the scan method giving the central dots and three inner ellipses,

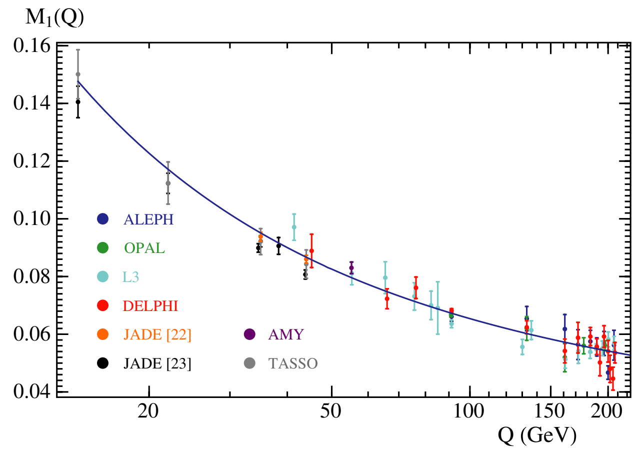

FIG. 10 (color online). Experimental data for the first moment of thrust. The solid line corresponds to the result from the first row of Table IV, and uses a fixed order code with power corrections in a renormalon-free scheme, but no resummation (neither QED nor bottom mass corrections).

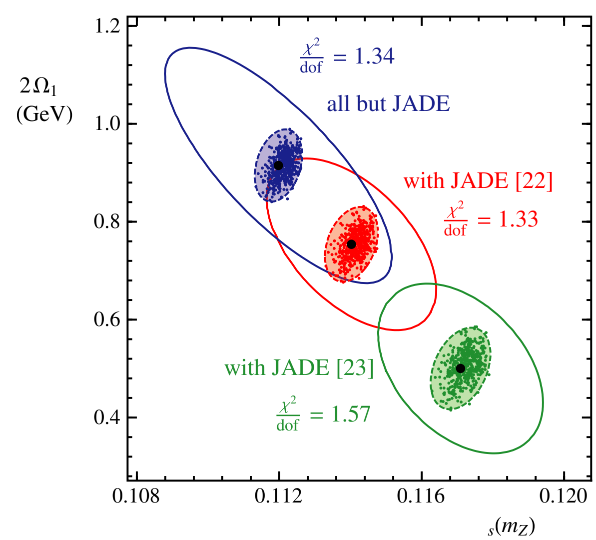

FIG. 11 (color online). Fit results when using ALEPH, DELPHI, OPAL, L3, AMY, TASSO, but no JADE data (upper blue ellipse), when also including JADE data from Ref. [22] (red central ellipse) [our default data set], and when instead including the JADE data from Ref. [23] (green lower ellipse). The ellipses here correspond to 1-σ for two parameters (68% C.L.).

[9]On the experimental side, Ref. [48] uses only the new JADE data from Ref. [23] and OPAL data. In our analysis the new JADE was excluded, but we utilized a larger data set that includes ALEPH, OPAL, L3, DELPHI, AMY, TASSO, and older JADE data. This may have a nonnegligible impact on the outcome of the comparison.

while the outer three ellipses show the respective combined 1-σ total experimental and theoretical uncertainties. Using all experimental data but excluding JADE measurements entirely gives the fit result shown by the upper blue ellipse. This result is compatible at 1-σ with the central red ellipse which shows our default analysis, using Ref. [22] JADE M_1 measurements. Replacing these two JADE data points by the four $Q > 22$ GeV JADE M_1 results from Ref. [23] yields the lower green ellipse (whose center is $\simeq 1.5$-σ from the central ellipse). For this fit the $\chi^2/\mathrm{d.o.f.}$ increases from 1.33 to 1.52 demonstrating that there is less compatibility between the data. For this reason, together with the concern about the impact of removing primary $b\bar{b}$ events with Monte Carlo simulations, we have used only JADE data from Ref. [22] in our main analysis.

A similar pattern is observed using the fixed order fits of M_1 discussed in Sec. IV. In this case, it is also straightforward to include the $Q = 14$, 22 GeV JADE data from Ref. [23]. If these two points are added to our default data set (which contains $Q = 35$ and 45 GeV as the lowest Q results for M_1) then we find $\alpha_s(m_Z) = 0.1155 \pm 0.0012$ and $\Omega_1 = 0.361 \pm 0.035$ GeV with $\chi^2/\mathrm{d.o.f.} = 1.3$. This is compatible at 1-σ with our final pure QCD result in Table I. If we include the entire set of JADE data from Ref. [23] instead of those from Ref. [22] then we find $\alpha_s(m_Z) = 0.1166 \pm 0.0012$ and $\Omega_1 = 0.306 \pm 0.033$ GeV with $\chi^2/\mathrm{d.o.f.} = 1.6$, very similar to the values observed for the green lower ellipse in Fig. 11. Hence, overall the fixed order analysis does not change the comparison of fits with the two different JADE data sets.

VI. HIGHER MOMENT ANALYSIS

In this section, we consider higher moments, $M_{n\geq 2}$, which have been measured experimentally up to $n = 5$. From Eq. (21) we see that these moments have power corrections $\propto 1/Q^k$ for $k \geq 1$. Since for the perturbative moments we have $\hat{M}_n/\hat{M}_{n+1} \simeq 4$–9, we estimate that the $1/Q^2$ power corrections are suppressed by $9\Lambda_{\mathrm{QCD}}/Q$ which varies from 1/8 to 1/44 for the Q values in our data set, $Q \geq 35$ GeV. Hence, for the analysis in this section, we can safely drop the $1/Q^2$ and higher power corrections and use the form

$$M_n = \hat{M}_n + \frac{2n\Omega_1}{Q}\hat{M}_{n-1}. \quad (39)$$

By using our fit results for $\alpha_s(m_Z)$ and Ω_1 from Eq. (34) we can directly make predictions for the moments $M_{2,3,4,5}$. This tests how well the theory does at calculating the perturbative contributions $\hat{M}_{2,3,4,5}$. The results for these moments are shown in Fig. 12 and correspond to $\chi^2/\mathrm{d.o.f.} = 1.3, 2.5, 0.8, 1.1$ for $n = 2, 3, 4, 5$ respectively, indicating that our formalism does quite well at reproducing these moments. The larger $\chi^2/\mathrm{d.o.f.}$ for $n = 3$ is related to a quite significant spread in the experimental data for this moment at $Q \gtrsim 190$ GeV. Note that we also see that the relation $M_n/M_{n+1} \simeq 4$–9 is satisfied by the experimental moments.

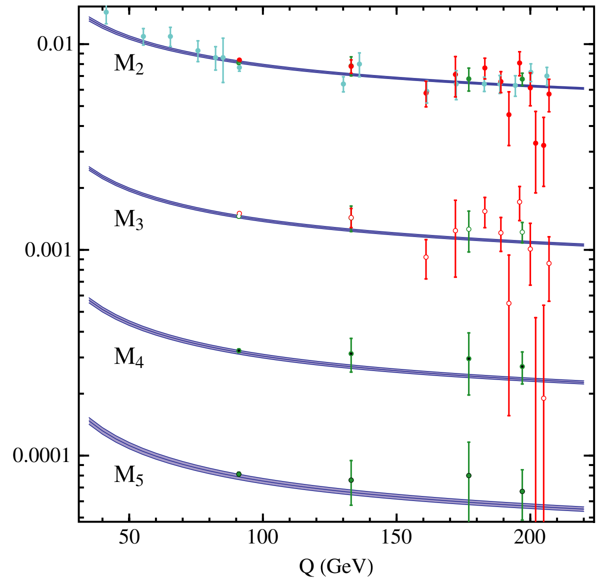

FIG. 12 (color online). Predictions for the higher moments M_2, M_3, M_4, M_5 using the best fit values from Eq. (34), and our full N^{3}LL + $\mathcal{O}(\alpha_s^3)$ code in the Rgap scheme, but with QED and mass effects turned off. The central points use different symbols for different moments.

An alternate way to test the higher moments is to perform a fit to this data. Since we have excluded the new

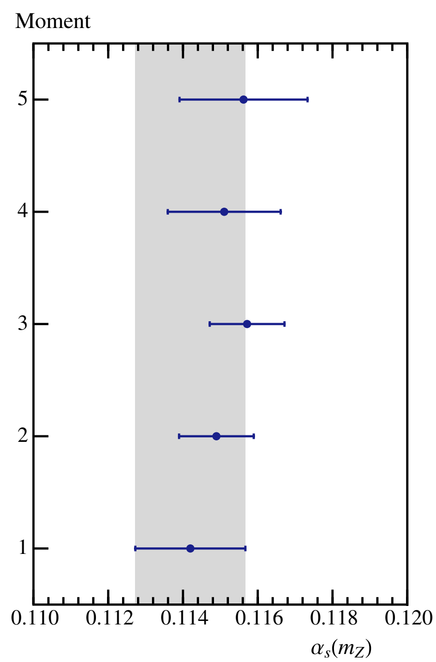

FIG. 13 (color online). One-parameter fits for $\alpha_s(m_Z)$ to the first five moments. We use our full set up with power corrections and renormalon subtractions, but with QED and mass corrections turned off. The value of Ω_1 is fixed from Eq. (34). The error bars include theoretical and experimental errors added in quadrature (not including uncertainty in Ω_1).

TABLE VI. Numerical results for α_s from one-parameter fits to the M_n moments. The second column gives the central values for $\alpha_s(m_Z)$, the third and fourth show the theoretical and experimental errors, respectively. Since Ω_1 was fixed for this analysis we do not quote a hadronization error.

n	$\alpha_s(m_Z)$	$\Delta_{\rm th}[\alpha_s]$	$\Delta_{\rm exp}[\alpha_s]$	$\chi^2/{\rm dof}$
2	0.1149	0.0009	0.0005	1.24
3	0.1157	0.0009	0.0005	1.87
4	0.1151	0.0011	0.0010	0.39
5	0.1156	0.0015	0.0010	0.23

JADE data in Ref. [23], we do not have a significant data set at smaller Q values for the higher moments. With our higher moment data set the degeneracy between $\alpha_s(m_Z)$ and Ω_1 is not broken for $n \geq 2$, and one finds very large experimental errors for a two-parameter fit already at $n = 2$. However we can still fit for $\alpha_s(m_Z)$ from data for each individual $M_{n\geq 2}$ by fixing the value of Ω_1 to the best fit value in Eq. (34) from our fit to M_1. For this exercise we use our full N^{3}LL + $\mathcal{O}(\alpha_s^3)$ code, but with QED and mass effects turned off. The outcome is shown in Fig. 13 and Table VI. We find only a little dependence of α_s on n, and all values are compatible with the fit to the first moment within less than 1-σ. This again confirms that our value for Ω_1 and perturbative predictions for $\hat{M}_{n\geq 2}$ are consistent with the higher moment data.

In Ref. [48] a two-parameter fit to higher thrust moments was carried out using OPAL data and the latest low energy JADE data. For $n = 2$ to $n = 5$ the results increase linearly from $\alpha_s(m_Z) = 0.1202 \pm (0.0018)_{\rm exp} \pm (0.0046)_{\rm th}$ to $\alpha_s(m_Z) = 0.1294 \pm (0.0027)_{\rm exp} \pm (0.0070)_{\rm th}$ respectively, and the weighted average for the first five moments of thrust is $\alpha_s(m_Z) = 0.1208 \pm 0.0018_{\rm exp} \pm 0.0045_{\rm th}$. The results are fully compatible within the uncertainties, and there is an indication of a trend towards larger $\alpha_s(m_Z)$ extracted from higher moments. In our analysis we do not observe this trend, but our results should not be directly compared since we have only performed a one parameter fit. After further averaging over results obtained from event shapes other than thrust Ref. [48] obtained as their final result $\alpha_s(m_Z) = 0.1153 \pm 0.0017_{\rm exp} \pm 0.0023_{\rm th}$. This is again perfectly compatible with our result in Eq. (34).

VII. HIGHER POWER CORRECTIONS FROM CUMULANT MOMENTS

In this section, we use cumulant moments as defined in Eq. (27) to discuss the presence of higher power corrections and their constraints from experimental data. There are two types of power corrections that are relevant for the cumulants, those defined rigorously by QCD matrix elements which come from the leading thrust factorization theorem, Ω'_n, and those from our simple parametrization of higher order power corrections in Eq. (15), $\Omega_{n,j\geq 1}$. For the latter a systematic matching onto QCD matrix elements has not been carried out and the corresponding perturbative coefficients have not been determined.

For the second cumulant M'_2 both types of power correction contribute to the leading $1/Q^2$ term in the combination

$$\tilde{\Omega}'_2 = \Omega'_2 + \bar{M}_{1,1}\Omega_{1,1}. \tag{40}$$

Without a calculation of the perturbative coefficient $\bar{M}_{1,1}$ we cannot argue that either one dominates, and hence we keep both of them. In terms of this parameter the OPE with its leading power correction for the second cumulant becomes simply

$$M'_2 = \hat{M}'_2 + \frac{4\tilde{\Omega}'_2}{Q^2}, \tag{41}$$

where $\hat{M}'_2$ is computed from our leading order factorization theorem, see Eq. (11). For the third cumulant M'_3 the power correction from the leading thrust factorization theorem is $1/Q^3$, while that from the subleading factorization theorem is $1/Q^2$, so

$$M'_3 = \hat{M}'_3 + \frac{6\bar{M}_{2,1}\Omega_{1,1}}{Q^2} + \frac{8\Omega'_3}{Q^3}, \tag{42}$$

where we keep both of these power corrections.

For our analysis we assume that the perturbative coefficients $\bar{M}_{1,1}$ and $\bar{M}_{2,1}$ get contributions at tree level, and hence that their logarithmic dependence on Q is α_s suppressed. Thus for fits to M'_2 and M'_3 we consider the three parameters $\tilde{\Omega}'_2$, $\bar{M}_{2,1}\Omega_{1,1}$, and Ω'_3. Our theoretical expectations are that $(\Omega'_n)^{1/n} \sim \Lambda_{\rm QCD}$ and $(\Omega_{1,1})^{1/2} \sim (\Omega'_n)^{1/n}$.

Since most of the experimental collaborations provide measurements only for moments we computed the cumulants using Eq. (3). To propagate the errors to the nth cumulant one needs the correlations between the first n moments, both statistical and systematical. Following experimental procedures we estimate the statistical correlation matrix from Monte Carlo simulations. These matrices are provided in Ref. [65] for $Q = 14$, 91.3, 206.6 GeV.[10] The computation of these matrices does not depend on the simulation of the detector and hence can be a priory employed on the data provided by any experimental collaboration. It was found that statistical correlation matrices depend very mildly on the center of mass energy, and our approach is to use the matrix computed at 14 GeV for $Q < 60$ GeV, the one computed at 91.3 for 60 GeV $\leq Q < 120$ GeV and the one at 206.6 GeV for $Q \geq 120$ GeV. The systematic correlation matrix for the moments is estimated using the minimal overlap model based on the systematic uncertainties, and then converted to uncertainties for the cumulants. We use this method even for the few cases in which experimental collaborations provide uncertainties for the cumulants directly, since we

[10] We thank Christoph Pahl for providing details on the use of correlation matrices for moments.

want to treat all data on the same footing. In these cases we have checked that the results are very similar.

To some extent the prescription we employ lies in between two extreme situations: (a) moments are completely uncorrelated, and (b) cumulants are completely uncorrelated. Situation (a) corresponds to the naive assumption that the moments are independent. Situation (b) is motivated by considering that properties like the location of the peak of the distribution ($\sim M_1$), the width of the peak ($\sim M_2'$), etc. are independent pieces of information. By assuming moments are uncorrelated one overestimates the errors of the cumulants. This would translate into larger experimental errors for our fit results and very small χ^2/d.o.f. Assuming that cumulants are uncorrelated induces very strong positive correlations between moments, which then leads to small uncertainties for the cumulants, especially for the variance, and larger χ^2/d.o.f. values. With the adopted prescription we use one finds a weaker positive correlation among moments, which translates into a situation between these two extremes.[11]

For our analysis we use our highest order code as described in Sec. III, and take the value $\alpha_s(m_Z) = 0.1142$ obtained in our fit to the first moment data with this code (see Table I). Since we are analyzing cumulants $M'_{n\geq 2}$ the value of Ω_1 is not required, and there is no distinction between having this parameter in $\overline{\text{MS}}$ or the Rgap scheme. Hence in order to fit for higher power corrections we use our purely perturbative code in the $\overline{\text{MS}}$ scheme. Thus all of the power correction parameters extracted in this section are in the $\overline{\text{MS}}$ scheme. The perturbative error is estimated as in Sec. III, by a 500 point scan of theory parameters (see the Appendix).

Before we fit for the higher power corrections, we will check how well our factorization theorem predicts the experimental cumulants using a simple exponential model for the nonperturbative soft function (the model with only one coefficient $c_0 = 1$ from Refs. [8,55]). This model has higher power corrections that are determined by its one parameter Ω_1 : $\Omega_2' = \Omega_1^2/4$, $\Omega_3' = \Omega_1^3/8$, $\Omega_4' = 3\Omega_1^4/32$, $\Omega_5' = 3\Omega_1^5/32$. Results are shown in Fig. 14, where good agreement between theory and data is observed.

For the M_n' in Fig. 14 we also observe that $M'_{n+1}/M'_n \sim 1/10$, so the $(n+1)$th order cumulant is generically one order of magnitude smaller than the nth order cumulant.

Next we will fit for the power correction parameters $\tilde{\Omega}_2'$, $\bar{M}_{2,1}\Omega_{1,1}$, and Ω_3'. For this analysis we neglect QED and b-mass effects. To facilitate this we consider the difference between the experimental cumulants M_n' and the

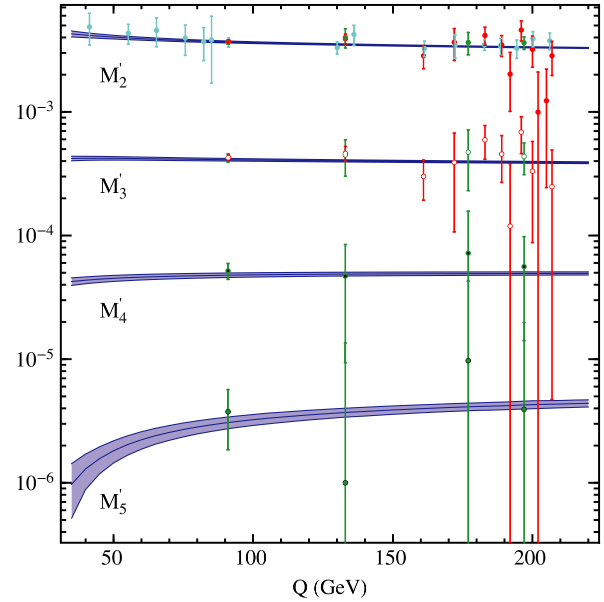

FIG. 14 (color online). Prediction of cumulants using our best-fit values for $\alpha_s(m_Z)$ and Ω_1 from the fit to the first thrust moment. The band includes only the theoretical uncertainty from the random scan. The theory prediction includes QED and mass corrections, in contrast to our numerical analysis which has no QED and b-mass effects and uses our default model, which translates into the following values for higher nonperturbative power corrections: $\Omega_2' = \Omega_1^2/4$, $\Omega_3' = \Omega_1^3/8$, $\Omega_4' = 3\Omega_1^4/32$, $\Omega_5' = 3\Omega_1^5/32$.

perturbative theoretical cumulants $\hat{M}_n'$, namely $M_2' - \hat{M}_2'$ and $M_3' - \hat{M}_3'$. From Eqs. (41) and (42) these differences are determined entirely by the power correction parameters we wish to fit. The results are shown in Table VII and the upper two panels of Fig. 15. From the $M_2' - \hat{M}_2'$ fit a fairly precise result is obtained for $(\tilde{\Omega}_2')^{1/2}$. Its central value of 740 MeV is compatible with $\sim 2\Lambda_{\text{QCD}}$, and hence agrees with naive dimensional analysis. Interestingly, we have checked that including a constant and $1/Q$ term in the second cumulant fit one finds that their coefficients are compatible with zero, in support of the theoretically expected $1/Q^2$ dependence.

For the fit to $M_3' - \hat{M}_3'$ there is a strong correlation between Ω_3' and $\bar{M}_{2,1}\Omega_{1,1}$ even though they occur at different orders in $1/Q$. Since the χ^2 is quadratic in these two parameters we can determine the linear combinations that exactly diagonalize their correlation matrix,

$$\begin{aligned}\Theta_2 &\equiv \bigg[\frac{6\bar{M}_{2,1}}{0.07}\bigg]\frac{\Omega_{1,1}}{4} + (0.3105\ \text{GeV}^{-1})\Omega_3',\\ \Theta_3 &\equiv \Omega_3' - (0.3105\ \text{GeV})\bigg[\frac{6\bar{M}_{2,1}}{0.07}\bigg]\frac{\Omega_{1,1}}{4}.\end{aligned} \tag{43}$$

Note that these combinations arise solely from experimental data. We have presented the coefficients of these combinations grouping together a factor of

[11] One might also construct the correlation matrices using the statistical and systematic errors from the thrust distributions themselves. Bins in distributions are statistically independent and systematic correlations are estimated using the minimal overlap model. Unfortunately this can introduce biases, and we thank Christoph Pahl for clarifying this point.

TABLE VII. Determination of power corrections from fits to M_2' and M_3'. All values in the table are in GeV. Columns two to four correspond to the central value, theoretical uncertainty, and experimental uncertainty, respectively (the latter includes both statistical and systematic errors added in quadrature). The values displayed correspond to the linear combinations in Eq. (43), which for M_3' diagonalize the experimental error matrix.

	Central	$\Delta_{\rm th}$	$\Delta_{\rm exp}$	$\frac{\chi^2}{\rm dof}$
$(\tilde{\Omega}_2')^{1/2}$	0.74	0.09	0.11	0.72
$(\Theta_2)^{1/2}$	1.21	0.10	0.22	0.93
$(\Theta_3)^{1/3}$	−2.61	0.15	1.51	

$(6\bar{M}_{2,1}/0.07)$, which is close to unity if $6\bar{M}_{2,1} \simeq \hat{M}_1$. The results in Table VII exhibit a reasonable uncertainty for Θ_2, but a large uncertainty for Θ_3. Hence, at this time it is not possible to determine the original parameters Ω_3' and $\bar{M}_{2,1}\Omega_{1,1}$ independently. As in the previous case, the fit does not exhibit any evidence for a $1/Q$ correction, confirming the theoretical prediction for this cumulant.

In Fig. 15, we also show results for cumulant differences $M_n' - \hat{M}_n'$ versus Q for $n = 4$ and $n = 5$. In all cases $n = 2, 3, 4, 5$ the perturbative cumulants $\hat{M}_n'$ are the largest component of the cumulant moments M_n', as can be verified by the reduction of the values by a factor of 2–3 in Fig. 15 compared to the values in Fig. 14. We also observe an order of magnitude suppression between the $(n+1)$th and nth terms, $(M_{n+1}' - \hat{M}_{n+1}')/(M_n' - \hat{M}_n') \sim 1/10$. For $n = 4, 5$ the OPE formula in Eq. (27) involves both $2^n\Omega_n'/Q^n$ terms and terms with nontrivial perturbative coefficients: $(2n\bar{M}_{n-1,1}\Omega_{1,1})/Q^2 + \ldots$ (where here the ellipses are terms at $1/Q^3$ and beyond). If the former dominated we would expect a suppression by $2\Lambda_{\rm QCD}/Q$ for the $(n+1)$th versus nth term. The observed suppression by $1/10$ is less strong and is instead consistent with domination by the $1/Q^2$ power correction terms in the $n = 4, 5$ cumulant differences. This would imply $[(n+1)\bar{M}_{n,1}]/[n\bar{M}_{n-1,1}] \sim 1/10$ and could in principle be verified by an explicit computation of these coefficients. In Fig. 15, we show fits to a $1/Q^2$ power correction, which are essentially dominated by the lowest energy point at the Z pole.

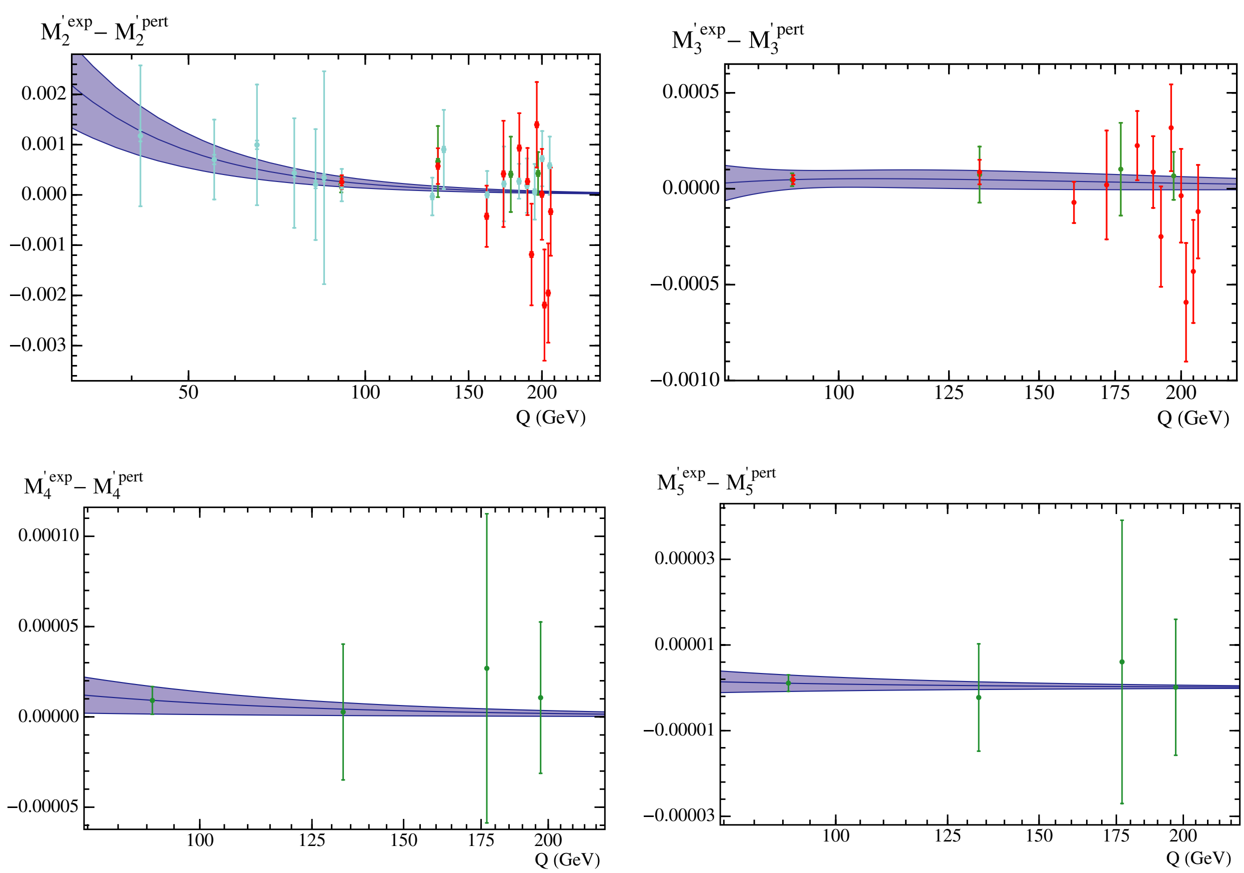

FIG. 15 (color online). Determination of power corrections from fits to data. On the vertical axes we display the nth experimental cumulant with the perturbative part subtracted $M_n' - \hat{M}_n'$. The error bars shown are experimental (statistical and systematic combined) added in quadrature with perturbative errors from the random scan over the profile parameters. The top-left panel shows the fit to $\tilde{\Omega}_2'/Q^2$, and the top-right panel shows the fit to $\bar{M}_{2,1}\Omega_{1,1}/Q^2$ and Ω_3'/Q^3 through the linear combinations in $\Theta_{2,3}$. The bottom two panels for $n = 4, 5$ show a simple fit to $\bar{M}_{3,1}\Omega_{1,1}$ and $\bar{M}_{4,1}\Omega_{1,1}$ taking $\Omega_4' = \Omega_5' = 0$.

The results are $\sqrt{8\bar{M}_{3,1}\Omega_{1,1}} = 0.20 \pm 0.08$ from fits to M_4' and $\sqrt{10\bar{M}_{4,1}\Omega_{1,1}} = 0.07 \pm 0.06$ from fits to M_5'. These values agree with our expectation of the $\sim 1/10$ suppression between the two $\bar{M}_{n,1}$ perturbative coefficients.

In this section, we have determined the $1/Q^2$ power correction parameter $\tilde{\Omega}_2'$ with 25% accuracy, and find it is 3.8σ different from zero. For the higher moments there are important contributions from a $\Omega_{1,1}/Q^2$ power correction, which appears to even dominate for $n \geq 4$. Clearly experimental data supports the pattern expected from the OPE relation in Eq. (27).

VIII. CONCLUSIONS

In this work, we have used a full τ-distribution factorization formula developed by the authors in a previous publication [8] to study moments and cumulant moments (cumulants) of the thrust distribution. Perturbatively it incorporates $\mathcal{O}(\alpha_s^3)$ matrix elements and nonsingular terms, a resummation of large logarithms, $\ln^k\tau$, to N^{3}LL accuracy, and the leading QED and bottom mass corrections. It also describes the dominant nonperturbative corrections, is free of the leading renormalon ambiguity, and sums up large logs appearing in perturbative renormalon subtractions.

Theoretically there are no large logs in the perturbative expression of the thrust moments, and when normalized in the same way the perturbative result from the full τ code with resummation agrees very well with the fixed order results. Nevertheless, when the code is properly self-normalized it significantly improves the order-by-order perturbative convergence towards the $\mathcal{O}(\alpha_s^3)$ result. In particular, the results remain within the perturbative error band of the previous order, in contrast to what is observed using fixed order expressions. This lends support to the theoretical uncertainty analysis from the code with resummation.

From fits to the first moment of the thrust distribution, M_1, we find the results for $\alpha_s(m_Z)$ and the leading power correction parameter Ω_1 given in Eq. (34). They are in nice agreement with values from the fit to the tail of the thrust distribution in Ref. [8]. The moment results have larger experimental uncertainties, and these dominate over theoretical uncertainties, in contrast with the situation in the tail region analysis of Ref. [8]. Repeating the M_1 fit using a fixed order code with no $\ln\tau$ resummation, but still retaining the summation of large logs in the perturbative renormalon subtractions, yields fully compatible results for $\alpha_s(m_Z)$ and Ω_1.

Using a Fourier-space operator product expansion we have parametrized higher order power corrections which are beyond the leading factorization formula, and analyzed the OPE both for moments M_n and cumulants M_n'. In the moments M_n the Ω_1/Q power correction from the leading factorization theorem enters with a perturbative suppression in its coefficient, and dominates numerically over higher $1/Q$ corrections. In contrast, the cumulants $M_{n\geq 2}'$ depend on higher order cumulant power corrections Ω_n'/Q^n from the leading factorization theorem, and are independent of $\Omega_1/Q, \ldots, \Omega_{n-1}'/Q^{n-1}$. Data on these cumulants appear to indicate that they receive important contributions from a $1/Q^2$ power correction that enters at a level beyond the leading thrust factorization theorem. Thus the OPE reveals that cumulants are appealing quantities for exploring subleading power corrections. We performed a fit to the second cumulant and determined a nonvanishing $\tilde{\Omega}_2'/Q^2$ power correction with a precision of 25%.

It would be interesting to extend the analysis performed here, based on OPE formulas related to factorization theorems, to other event-shape moments and cumulants. Examples of interest include the heavy jet mass event shape [7,66–69], angularities [70,71], as well as more exclusive event shapes like jet broadening [72–76]. Other event-shape moments were considered at $\mathcal{O}(\alpha_s^3)$ in Ref. [48] in the context of the dispersive model for the $1/Q$ power corrections.

ACKNOWLEDGMENTS

This work was supported in part by the Office of Nuclear Physics of the U.S. Department of Energy under Contracts No. DE-FG02-94ER40818, No. DE-FG02-06ER41449, the European Community's Marie-Curie Research Networks under Contract No. MRTN-CT-2006-035482 (FLAVIAnet), MRTN-CT-2006-035505 (HEPTOOLS) and PITN-GA-2010-264564 (LHCphenOnet), and the U.S. National Science Foundation, Grant No. NSF-PHY-0969510 (LHC Theory Initiative). V. M. has been supported in part by a Marie Curie Fellowship under Contract No. PIOF-GA-2009-251174, and I. S. in part from the Alexander von Humboldt foundation. V. M., I. S. and A. H. H. are also supported in part by MISTI global seed funds. We thank C. Pahl for useful discussions concerning the treatment of JADE experimental data. M. F. thanks S. Fleming for discussions.

APPENDIX: THEORY PARAMETER SCAN

In this appendix we describe the method we use to estimate uncertainties in our analysis. We will briefly review the profile functions and the theoretical parameters which determine the theory uncertainty. We will also describe the scan over those parameters and the effects they have on the fit results.

The profile functions used in Ref. [8], to which we refer for a more extensive description, are τ-dependent factorization scales which allow us to smoothly interpolate between the theoretical constraints the hard, jet and soft scale must obey in different regions of the thrust distribution:

$$
\begin{aligned}
&(1)\,\text{peak: } \mu_H \sim Q, \quad \mu_J \sim \sqrt{\Lambda_{\rm QCD} Q}, \quad \mu_S \gtrsim \Lambda_{\rm QCD},\\
&(2)\,\text{tail: } \mu_H \sim Q, \quad \mu_J \sim Q\sqrt{\tau}, \quad \mu_S \sim Q\tau, \qquad\qquad (A1)\\
&(3)\,\text{far tail: } \mu_H = \mu_J = \mu_S \sim Q.
\end{aligned}
$$

The factorization theorem derived for thrust in Ref. [8] is formally invariant under $\mathcal{O}(1)$ changes of the profile function scales. The residual dependence on the choice of profile functions constitutes one part of the theoretical uncertainties and provides a method to estimate higher order perturbative corrections. We adopt a set of six parameters that can be varied in our theory error analysis which encode this residual freedom while still satisfying the constraints in Eq. (A1).

For the profile function at the hard scale, we adopt

$$\mu_H = e_H Q, \qquad (A2)$$

where e_H is a free parameter which we vary from $1/2$ to 2 in our theory error analysis.

For the soft profile function we use the form

$$\mu_S(\tau) = \begin{cases} \mu_0 + \frac{b}{2t_1}\tau^2, & 0 \le \tau \le t_1,\\ b\tau + d, & t_1 \le \tau \le t_2,\\ \mu_H - \frac{b}{1-2t_2}\left(\frac{1}{2}-\tau\right)^2, & t_2 \le \tau \le \frac{1}{2}. \end{cases} \qquad (A3)$$

Here, t_1 and t_2 represent the borders between the peak, tail and far-tail regions. μ_0 is the value of μ_S at $\tau = 0$. Since the thrust value where the peak region ends and the tail region begins is Q dependent, $t_1 \simeq 1/Q$, we define the Q-independent parameter n_1 by $t_1 = n_1/(Q/1\ \text{GeV})$. To ensure that $\mu_S(\tau)$ is a smooth function, the quadratic and linear forms are joined by demanding continuity of the function and its first derivative at $\tau = t_1$ and $\tau = t_2$, which fixes $b = 2(\mu_H - \mu_0)/(t_2 - t_1 + \frac{1}{2})$ and $d = [\mu_0(t_2 + \frac{1}{2}) - \mu_H t_1]/(t_2 - t_1 + \frac{1}{2})$. In our theory error analysis we vary the free parameters n_1, t_2 and μ_0.

The profile function for the jet scale is determined by the natural relation between the hard, jet, and soft scales

$$\mu_J(\tau) = \left(1 + e_J\left(\frac{1}{2}-\tau\right)^2\right)\sqrt{\mu_H \mu_S(\tau)}. \qquad (A4)$$

The term involving the free $\mathcal{O}(1)$ parameter e_J implements a modification to this relation and vanishes in the multijet region where $\tau = 1/2$. We use a variation of e_J to include the effect of such modifications in our estimation of the theoretical uncertainties.

In our theory error analysis we vary $\mu_{\rm ns}$ to account for our ignorance on the resummation of logarithms of τ in the nonsingular corrections. We consider three possibilities

$$\mu_{\rm ns}(\tau) = \begin{cases} \mu_H, & n_s = 1,\\ \mu_J(\tau), & n_s = 0,\\ \frac{1}{2}[\mu_J(\tau) + \mu_S(\tau)], & n_s = -1. \end{cases} \qquad (A5)$$

The complete set of theoretical parameters and the their ranges of variation are summarized in Table VIII.

Besides the parameters associated with the profile functions, the other theory parameters are $\Gamma_3^{\rm cusp}$, j_3, s_3, and $\epsilon_{2,3}$. The cusp anomalous dimension at $\mathcal{O}(\alpha_s^4)$, $\Gamma_3^{\rm cusp}$ is estimated via Padé approximants and we assign a 200% uncertainty to this approximation. j_3 and s_3 represent the nonlogarithmic three-loop term in the position-space hemisphere jet and soft functions, respectively. These two parameters and their variations are estimated via Padé approximations. The last two parameters ϵ_2 and ϵ_3 allow us to include the statistical errors in the numerical determination of the nonsingular distribution at two (from EVENT2 [77,78]) and three (from EERAD3 [2]) loops, respectively.

At each order we randomly scan the parameter space summarized in Table VIII with a uniform measure, extracting 500 points. Each of the points in Fig. 6 is the result of the fit performed with a single choice of a point in the parameter space. The contour of the area in the α_s-$2\Omega_1$ plane covered by the fit results at each given order is fitted to an ellipse, which is interpreted as a 1-σ theoretical uncertainty. The ellipse is determined as follows: in a first step we determine the outermost points on the α_s-$2\Omega_1$ plane (defined by the outermost convex polygon). We then perform a fit to these points using a χ^2 which is the square of the formula for an ellipse,

$$\chi^2_{\rm ellipse} = \sum_i [a(\alpha_i - \alpha_0)^2 + 4b(\Omega_i - \Omega_0)^2 + 2c(\alpha_i - \alpha_0)(\Omega_i - \Omega_0) - 1]^2. \qquad (A6)$$

Here the sum is over the outermost points. The coordinates for the center of the ellipse, α_0 and Ω_0, are fixed ahead of time to the average of the maximum and minimum values of $\alpha_s(m_Z)$ and Ω_1 in the scan. We then minimize $\chi^2_{\rm ellipse}$ to determine the parameters a, b, c of the ellipse.

TABLE VIII. Theory parameters relevant for estimating the theory uncertainty, their default values and range of values used for the theory scan during the fit procedure.

Parameter	Default value	Range of values
μ_0	2 GeV	1.5 to 2.5 GeV
n_1	5	2 to 8
t_2	0.25	0.20 to 0.30
e_J	0	-1, 0, 1
e_H	1	0.5 to 2.0
n_s	0	-1, 0, 1
$\Gamma_3^{\rm cusp}$	1553.06	-1553.06 to $+4659.18$
j_3	0	-3000 to $+3000$
s_3	0	-500 to $+500$
ϵ_2	0	-1, 0, 1
ϵ_3	0	-1, 0, 1

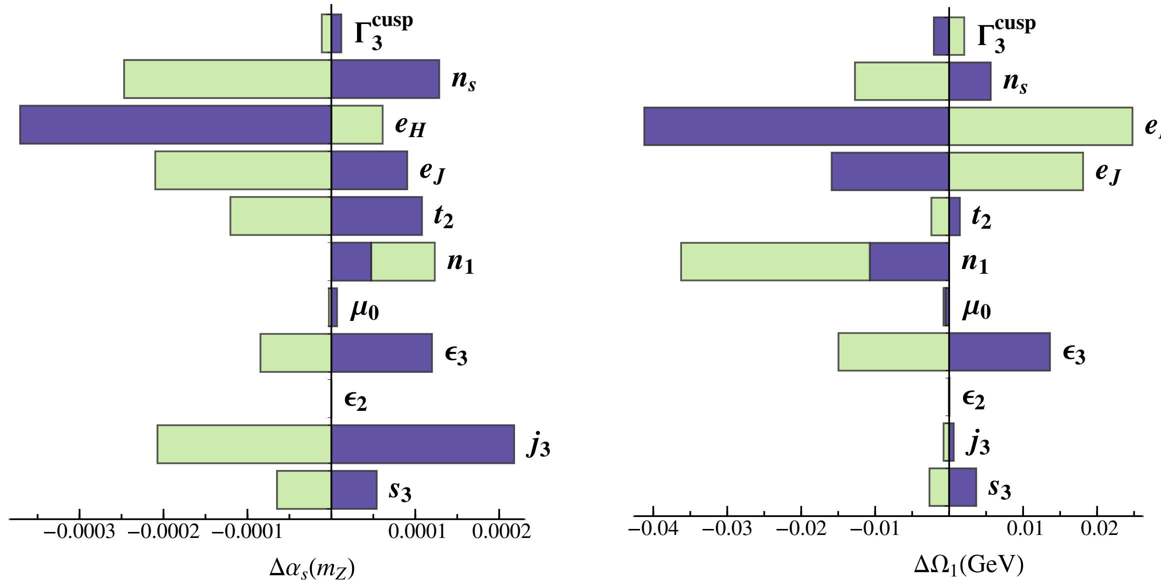

FIG. 16 (color online). Impact on parameters of the M_1 fit from variations of the best-fit values for $\alpha_s(m_Z)$ and Ω_1 values in the ranges given in Table VIII. The dark shaded blue regions represent values of the parameters larger than their default values, the light shaded green regions where the parameters are smaller than their default values.

One could further express the coefficients a and b by

$$a = \frac{1 + \sqrt{1 + 4c^2\Delta\alpha^2\Delta\Omega^2}}{2\Delta\alpha^2}, \qquad b = \frac{1 + \sqrt{1 + 4c^2\Delta\alpha^2\Delta\Omega^2}}{8\Delta\Omega^2}, \tag{A7}$$

where $\Delta\alpha$ and $\Delta\Omega$ are just the half of the difference of the maximum and minimum values of $\alpha_s(m_Z)$ and Ω_1, respectively, on the ellipse. Setting $\Delta\alpha$ and $\Delta\Omega$ to the corresponding values obtained from the fit points of the scan (i.e., the perturbative errors) the coefficients a and b can be fixed and only c remains as a free parameter. The minimization of $\chi^2_{\mathrm{ellipse}}$ in Eq. (A6) gives almost identical results regardless of whether or not Eqs. (A7) are imposed.

In Fig. 16, we vary a single parameter of Table VIII keeping all the others fixed at their respective default values, and we plot the change of $\alpha_s(m_Z)$ and Ω_1 as compared to the values obtained from the first moment thrust fit with the default setup. In the figure, the dark shaded blue area represents a variation where the parameter is larger than the default value, and the light shaded green one where the parameter is smaller. The largest uncertainty is associated with the variation of the hard scale, e_H. The value of $\alpha_s(m_Z)$ is similarly affected by the uncertainty of the profile function parameters, the statistical error from the numerical determination of the three-loop nonsingular distribution from EERAD3 [2], and by the parameter j_3. It is rather insensitive to the variation of the four-loop cusp anomalous dimension and the statistical error from the determination of the two-loop nonsingular contribution to the thrust distribution. The value of Ω_1 is mainly sensitive to the profile function parameters and ϵ_3, but is quite insensitive to j_3.

[1] S. Kluth, Rep. Prog. Phys. **69**, 1771 (2006).
[2] A. Gehrmann-De Ridder, T. Gehrmann, E. W. N. Glover, and G. Heinrich, Phys. Rev. Lett. **99**, 132002 (2007).
[3] A. Gehrmann-De Ridder, T. Gehrmann, E. W. N. Glover, and G. Heinrich, J. High Energy Phys. 12 (2007) 094.
[4] S. Weinzierl, Phys. Rev. Lett. **101**, 162001 (2008).
[5] S. Weinzierl, J. High Energy Phys. 06 (2009) 041.
[6] T. Becher and M. D. Schwartz, J. High Energy Phys. 07 (2008) 034.
[7] Y.-T. Chien and M. D. Schwartz, J. High Energy Phys. 08 (2010) 058.
[8] R. Abbate, M. Fickinger, A. H. Hoang, V. Mateu, and I. W. Stewart, Phys. Rev. D **83**, 074021 (2011).
[9] E. Farhi, Phys. Rev. Lett. **39**, 1587 (1977).
[10] C. W. Bauer, S. Fleming, and M. E. Luke, Phys. Rev. D **63**, 014006 (2001).
[11] C. W. Bauer, S. Fleming, D. Pirjol, and I. W. Stewart, Phys. Rev. D **63**, 114020 (2001).

[12] C. W. Bauer and I. W. Stewart, Phys. Lett. B **516**, 134 (2001).
[13] C. W. Bauer, D. Pirjol, and I. W. Stewart, Phys. Rev. D **65**, 054022 (2002).
[14] C. W. Bauer, S. Fleming, D. Pirjol, I. Z. Rothstein, and I. W. Stewart, Phys. Rev. D **66**, 014017 (2002).
[15] A. H. Hoang and I. W. Stewart, Phys. Lett. B **660**, 483 (2008).
[16] A. H. Hoang and S. Kluth, arXiv:0806.3852.
[17] A. H. Hoang, A. Jain, I. Scimemi, and I. W. Stewart, Phys. Rev. Lett. **101**, 151602 (2008).
[18] A. H. Hoang, A. Jain, I. Scimemi, and I. W. Stewart, Phys. Rev. D **82**, 011501 (2010).
[19] S. Bethke, Eur. Phys. J. C **64**, 689 (2009).
[20] S. Bethke (unpublished).
[21] S. Bethke, A. H. Hoang, S. Kluth, J. Schieck, I. W. Stewart *et al.*, arXiv:1110.0016.
[22] P. A. Movilla Fernandez, O. Biebel, S. Bethke, S. Kluth, and P. Pfeifenschneider (JADE Collaboration), Eur. Phys. J. C **1**, 461 (1998).
[23] C. Pahl, S. Bethke, S. Kluth, and J. Schieck (JADE Collaboration), Eur. Phys. J. C **60**, 181 (2009).
[24] G. Abbiendi (OPAL Collaboration), Eur. Phys. J. C **40**, 287 (2005).
[25] K. Ackerstaff *et al.* (OPAL Collaboration), Z. Phys. C **75**, 193 (1997).
[26] A. Heister (ALEPH Collaboration), Eur. Phys. J. C **35**, 457 (2004).
[27] J. Abdallah *et al.* (DELPHI Collaboration), Eur. Phys. J. C **29**, 285 (2003).
[28] J. Abdallah (DELPHI Collaboration), Eur. Phys. J. C **37**, 1 (2004).
[29] P. Abreu *et al.* (DELPHI Collaboration), Phys. Lett. B **456**, 322 (1999).
[30] M. Acciarri *et al.* (L3 Collaboration), Phys. Lett. B **489**, 65 (2000).
[31] P. Achard *et al.* (L3 Collaboration), Phys. Rep. **399**, 71 (2004).
[32] W. Braunschweig *et al.* (TASSO Collaboration), Z. Phys. C **47**, 187 (1990).
[33] Y. K. Li *et al.* (AMY Collaboration), Phys. Rev. D **41**, 2675 (1990).
[34] A. Gehrmann-De Ridder, T. Gehrmann, E. Glover, and G. Heinrich, J. High Energy Phys. 05 (2009) 106.
[35] S. Weinzierl, Phys. Rev. D **80**, 094018 (2009).
[36] Y. L. Dokshitzer and B. R. Webber, Phys. Lett. B **352**, 451 (1995).
[37] R. Akhoury and V. I. Zakharov, Phys. Lett. B **357**, 646 (1995).
[38] R. Akhoury and V. I. Zakharov, Nucl. Phys. **B465**, 295 (1996).
[39] P. Nason and M. H. Seymour, Nucl. Phys. **B454**, 291 (1995).
[40] G. P. Korchemsky and G. Sterman, Nucl. Phys. **B437**, 415 (1995).
[41] M. Beneke, Phys. Rep. **317**, 1 (1999).
[42] E. Gardi, J. High Energy Phys. 04 (2000) 030.
[43] Y. L. Dokshitzer, G. Marchesini, and B. R. Webber, Nucl. Phys. **B469**, 93 (1996).
[44] Y. L. Dokshitzer, A. Lucenti, G. Marchesini, and G. Salam, J. High Energy Phys. 05 (1998) 003.
[45] E. Gardi and G. Grunberg, J. High Energy Phys. 11 (1999) 016.
[46] O. Biebel, Phys. Rep. **340**, 165 (2001).
[47] C. Pahl, S. Bethke, O. Biebel, S. Kluth, and J. Schieck, Eur. Phys. J. C **64**, 533 (2009).
[48] T. Gehrmann, M. Jaquier, and G. Luisoni, Eur. Phys. J. C **67**, 57 (2010).
[49] Y. L. Dokshitzer, A. Lucenti, G. Marchesini, and G. Salam, Nucl. Phys. **B511**, 396 (1998).
[50] Y. L. Dokshitzer and B. Webber, Phys. Lett. B **404**, 321 (1997).
[51] C. Lee and G. Sterman, arXiv:hep-ph/0603066.
[52] C. Lee and G. Sterman, Phys. Rev. D **75**, 014022 (2007).
[53] G. P. Korchemsky and G. Sterman, Nucl. Phys. **B555**, 335 (1999).
[54] G. P. Korchemsky and S. Tafat, J. High Energy Phys. 10 (2000) 010.
[55] Z. Ligeti, I. W. Stewart, and F. J. Tackmann, Phys. Rev. D **78**, 114014 (2008).
[56] K. S. M. Lee and I. W. Stewart, Nucl. Phys. **B721**, 325 (2005).
[57] C. W. Bauer, M. E. Luke, and T. Mannel, Phys. Rev. D **68**, 094001 (2003).
[58] C. W. Bauer, M. Luke, and T. Mannel, Phys. Lett. B **543**, 261 (2002).
[59] A. K. Leibovich, Z. Ligeti, and M. B. Wise, Phys. Lett. B **539**, 242 (2002).
[60] S. W. Bosch, M. Neubert, and G. Paz, J. High Energy Phys. 11 (2004) 073.
[61] M. Beneke, F. Campanario, T. Mannel, and B. Pecjak, J. High Energy Phys. 06 (2005) 071.
[62] R. Kelley, M. D. Schwartz, R. M. Schabinger, and H. X. Zhu, Phys. Rev. D **84**, 045022 (2011).
[63] A. Hornig, C. Lee, I. W. Stewart, J. R. Walsh, and S. Zuberi, J. High Energy Phys. 08 (2011) 054.
[64] P. F. Monni, T. Gehrmann, and G. Luisoni, J. High Energy Phys. 08 (2011) 010.
[65] C. Pahl, Ph.D. thesis, TU Munich, 2007.
[66] L. Clavelli, Phys. Lett. **85B**, 111 (1979).
[67] T. Chandramohan and L. Clavelli, Nucl. Phys. **B184**, 365 (1981).
[68] L. Clavelli and D. Wyler, Phys. Lett. **103B**, 383 (1981).
[69] S. Catani, G. Turnock, and B. Webber, Phys. Lett. B **272**, 368 (1991).
[70] C. F. Berger, T. Kúcs, and G. Sterman, Phys. Rev. D **68**, 014012 (2003).
[71] A. Hornig, C. Lee, and G. Ovanesyan, J. High Energy Phys. 05 (2009) 122.
[72] S. Catani, G. Turnock, and B. Webber, Phys. Lett. B **295**, 269 (1992).
[73] Y. L. Dokshitzer, A. Lucenti, G. Marchesini, and G. Salam, J. High Energy Phys. 01 (1998) 011.
[74] J.-y. Chiu, A. Jain, D. Neill, and I. Z. Rothstein, Phys. Rev. Lett. **108**, 151601 (2012).
[75] T. Becher, G. Bell, and M. Neubert, Phys. Lett. B **704**, 276 (2011).
[76] J.-Y. Chiu, A. Jain, D. Neill, and I. Z. Rothstein, J. High Energy Phys. 05 (2012) 084.
[77] S. Catani and M. H. Seymour, Phys. Lett. B **378**, 287 (1996).
[78] S. Catani and M. H. Seymour, Nucl. Phys. **B485**, 291 (1997).